# Structure and Dynamics of Axisymmetric Tornado-like Vortices Simulated with a Semislip Lower Boundary

STEFANO GIOVE,[a] RICHARD ROTUNNO,[b] CARLO CINTOLESI,[a] AND MARIO MARCELLO MIGLIETTA[c]

[a] *Department of Physics and Astronomy, University of Bologna, Bologna, Italy*
[b] *NSF National Center for Atmospheric Research, Boulder, Colorado*
[c] *National Research Council-Institute of Atmospheric Sciences and Climate, Padua, Italy*

ABSTRACT: No-slip boundary conditions are often employed in idealized axisymmetric models to study tornadoes. These boundary conditions result in a poor representation of near-ground winds, which are of crucial importance for tornadoes. In this study, the boundary layer of tornadoes is investigated using more realistic semislip conditions as the lower boundary of axisymmetric, idealized simulations. The drag law formulation of semislip conditions introduces the drag coefficient $C_d$ as a control parameter, alongside the swirl ratio $S_r$ (related to the system's rotation) and a Reynolds number (describing diffusive effects) already employed in previous studies employing no-slip conditions. The exploration of a wide range of $C_d$ values shows that the analytical two-tiered potential vortex boundary layer is preserved under semislip conditions. The lower tier becomes shallower as $C_d$ decreases, finally vanishing for $C_d = 0.001$. The drag coefficient plays a fundamental role in determining the structure of the vortex. A decrease in $C_d$ causes the same one-celled to two-celled transition previously observed for an increase of $S_r$ under no-slip conditions. For the range of swirl ratios and Reynolds numbers used in the present study, a decrease in $C_d$ leads to the intensification of the surface inflow and a reduced dissipation of angular momentum of parcels advected toward the center of the vortex. This intensification for decreasing $C_d$ occurs only for subcritical vortices; thus, the effect appears dependent on vortex structure and corner-flow swirl ratio.

KEYWORDS: Boundary layer; Tornadoes; Vortices; Boundary conditions

## 1. Introduction

Their intensity, small scale, and unpredictable nature hinder direct measurements of tornadoes. Hence, the study of the fluid dynamics of tornadoes has relied primarily on numerical simulations. The significant scale disparity with their parent supercell thunderstorm renders the study of tornadoes through three-dimensional storm models computationally expensive. As a result, axisymmetric, idealized models have been widely employed (Fiedler 1994, 1995; Nolan 2005; Rotunno et al. 2016), isolating the features of supercells that are important for tornadoes. Previous studies (Rotunno 2013; Rotunno et al. 2016) have shown that, under this idealized approach, the solutions depend on two nondimensional parameters: the swirl ratio $S_r$, related to the ratio of the circulation of the fluid to the upward forcing, and a Reynolds number Re, related to diffusive effects. In these studies, no-slip boundary conditions were employed, in which the surface wind is set to zero. This no-slip condition allowed the comparison of the simulations with the results of Burggraf et al. (1971), who studied the boundary layer of a potential vortex under a no-slip condition. The assumption of a potential vortex (a vortex with radially constant angular momentum) is often employed as a convenient simplification since natural

vortices like tornadoes and tropical cyclones show radial profiles of azimuthal velocity akin to potential vortices, from the radius of the maximum azimuthal velocity outward (Tanamachi et al. 2007).

The main limitation of no-slip boundary conditions is that by imposing the wind speed to be identically zero at the surface, the near-surface winds are poorly reproduced. These low-level winds are of crucial importance, since they damage structures, cause injuries and fatalities, and lead to significant economic losses (Smith and Matthews 2015; Ashley and Strader 2016). Motivated by these shortcomings, the objective of the present study is to investigate the boundary layer of idealized tornadoes under semislip boundary conditions, a more realistic approach between the no-slip and free-slip conditions usually employed. The significance of this objective is emphasized by recent Doppler on Wheels observations (Kosiba and Wurman 2023), which show that the strongest tornadic winds occur at the lowest levels (below 15 m). A similar result was obtained by Kosiba and Wurman (2013), who investigated the wind field of a tornado near Russell, Kansas, observing the peak wind intensity at ~5 m above ground level through a combination of radar, anemometer, and ground-based velocity track display (GBVTD).

The boundary layer of a potential vortex was shown to exhibit a two-tiered structure under no-slip conditions (Burggraf et al. 1971), with the lower frictional tier below an inviscid upper tier. The tiers are delimited by the maximum in $-ru$, where $u$ is the radial velocity and $r$ is the distance from the vortex center. With this work, we aim to determine the extent to which the analytically derived boundary layer structure is preserved under semislip conditions and, in particular, how

*Corresponding author*: Stefano Giove, stefano.giove@studio.unibo.it

the two-tiered structure evolves for decreasing values of the drag coefficient $C_d$.

Laboratory experiments (Ward 1972; Church et al. 1979) and no-slip idealized simulations (Rotunno et al. 2016) analyzed the dependence of the vortex structure on the nondimensional parameters. For low swirl ratios, the vortex attains a one-celled structure, with a single vortex featuring a central updraft starting from the surface and reaching the top of the domain. For larger $S_r$, the vortex undergoes an abrupt transition [vortex breakdown (vb)] at a certain height, with the updraft suddenly deviating outward due to the presence of a central downdraft. The interface between the updraft and downdraft shifts downward for a further increase in $S_r$. When the interface reaches the ground, the vortex attains a complete two-celled (2-c) structure, with a central downdraft surrounded by an updraft. For even larger $S_r$, the two-celled vortex breaks into multiple vortices revolving around a common center. Rotunno et al. (2016) explored extensively the $S_r$–Re parameter space, finding that the optimal vortices (vortices with the maximum pressure drop, occurring for vortex breakdown solutions) lie along the $S_r \propto \mathrm{Re}^{-1/3}$ diagonal line in the log–log $S_r$–Re space. The use of surface drag as the semislip boundary condition allows us to introduce the drag coefficient $C_d$ as a third control parameter. The goal of the present work is to assess whether $C_d$ plays a role in determining the vortex structure and its effect on the optimal vortex line in $S_r$–Re space.

The present study was motivated by Fiedler (2017), in which semislip lower boundary conditions were used for axisymmetric simulations of tornadoes. Fiedler (2017) comments on a simulation using an intermediate value of the drag parameter $\gamma$, "Note, unlike the simulations with larger values of $\gamma$, at $r = 0$, the updraft is slightly diminished from that in the surrounding core. This may seem paradoxical that this is happening with less friction, but the paradox perhaps could be resolved with an understanding of the boundary layer of a potential vortex . . . ." The objective of this study is to provide that understanding. Note that, in the present model, we use the nonlinear drag law and vary the drag parameter $C_d$ instead of the linearized version used in Fiedler (2017).

Along with idealized axisymmetric simulations, tornado dynamics has been investigated through three-dimensional simulations (Lewellen and Lewellen 2007a,b; Fiedler 2009). Lewellen et al. (2000) introduced a local measure of the swirl ratio in the corner flow region, the corner flow swirl ratio $S_c$. The authors showed the dependence of $S_c$ on surface roughness, among other parameters. Liu and Ishihara (2016) studied the influence of surface roughness on tornado-like vortices employing a large-eddy simulation (LES) approach (Wyngaard 2010) and using semislip conditions. Their results indicate that the vortex structure changes produced by an increase in roughness are similar to those observed for a decrease in the external swirl ratio. A number of other three-dimensional LES studies of idealized tornadoes employing semislip conditions have appeared in recent years (Bryan et al. 2017; Nolan et al. 2017; Wang et al. 2020). Wang et al. (2023), in particular, examined the effects of a parameterized frictional sublayer.

Some studies have adopted a different approach to investigate the effects of surface roughness on tornado-like vortices. Both numerical simulations (Gairola et al. 2023; Natarajan and Hangan 2012) and laboratory experiments (Neakrase and Greeley 2010) have modeled surface roughness based on the density and size of geometric obstacles.

On the opposite side of the spectrum compared to the idealized approach followed here, some individual simulations of supercells at resolutions fine enough to explicitly resolve tornadoes have been successfully run (Orf 2019; Xue et al. 2014). Notably, Orf et al. (2017) ran a simulation with 1.84 billion grid points, with an inner mesh with a grid spacing of 30 m, simulating the evolution of a long-track, damaging tornado.

The paper is organized as follows: section 2 describes the physical problem, while section 3 presents the governing equations and a description of the model setup. The results are presented and discussed in section 4. Finally, the conclusions are summarized in section 5.

## 2. Physical problem

The present study of the effects of semislip boundary conditions on supercell tornadoes is carried out considering an idealized supercell thunderstorm, which simplifies and isolates the characteristics that are among the critical ingredients for tornado formation and its features. Following the Fiedler chamber approach (Fiedler 1995), the supercell is idealized as a cylinder of radius $R$ and height $Z$. The domain rotates at the rate $\Omega$, producing an angular momentum distribution $\Omega r^2$. The fluid is vertically accelerated by a prescribed upward force per unit mass $F(r, z)$, defined as a surrogate for the thunderstorm's buoyancy. The Fiedler chamber approach allows us to assume axisymmetry, reducing the physical problem to only two dimensions, radial and vertical.

A schematic diagram of the domain used for the simulations is presented in Fig. 1, and the parameters characterizing the physical problem are summarized in Table 1. The physical problem is as in Rotunno et al. (2016), except for the lower boundary layer conditions. The $r = 0$ and $r = R$ boundaries are impermeable ($\mathbf{u} \cdot \mathbf{n} = 0$, where $\mathbf{u}$ is the fluid velocity and $\mathbf{n}$ is the normal to the boundary) free-slip walls, while the domain's top boundary ($z = Z$) is an impermeable no-slip wall. The defining feature of the present study is the use of semislip conditions for the domain's bottom boundary, where "semislip" refers to the use of a drag-force formulation of the surface shear stresses:

$$\tau_{i3} = \rho C_d u_i V = \rho C_d u_i \sqrt{u^2 + v^2}, \tag{1}$$

where $C_d$ is the drag coefficient and $V$ is the surface wind speed. We note that the present formulation is nonlinear, in contrast to the linear approach of Fiedler (2017) [his Eqs. (8)–(10)].

The prescribed upward forcing is active in an elliptically shaped region of vertical and horizontal semiaxes $l_z$ and $l_r$, respectively (Fig. 1). The maximum forcing is located at $(r, z) = (0, z_b)$, the center of the ellipse. Integrating vertically the upward force per unit mass for $r = 0$,
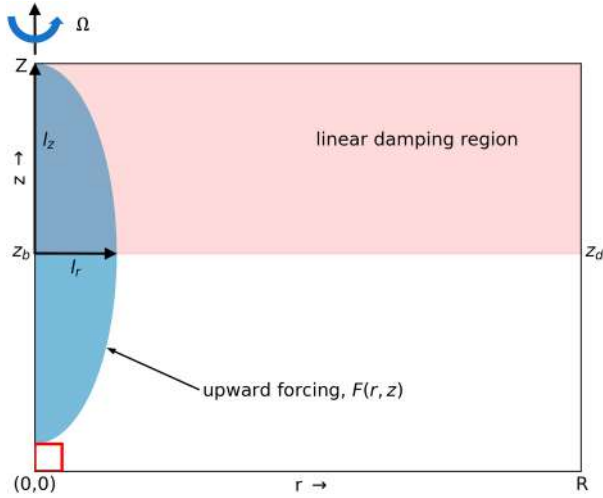
FIG. 1. Schematic diagram of the computational domain employed for the numerical simulations. The red square box is the 1 km × 1 km display domain used in Figs. 8, 9, 11, 12, and 14.

$$W^2 = \int_{z_b-l_z}^{z_b+l_z} 2F(0, z)dz, \qquad (2)$$

where $W$ is the forcing velocity, also called the thermodynamic speed limit, as it is the velocity that a parcel at rest at the bottom of the forcing region and for $r = 0$ would acquire at the top of the forcing region if buoyancy were the only force acting on it (Fiedler 1994). The forcing $F(r, z)$ is tuned so that $W = 80$ m s$^{-1}$.

To prevent numerical disturbances produced at the domain top from recirculating and reaching the vortex below, a damping layer is introduced above the height $z_d$. In particular, the damping is a linear relaxation, with time constant $\tau = 100$ s. Figure 1 shows that the updraft forcing region and the damping layer overlap, which implies that the forcing velocity must be corrected, taking into account the role of the damping layer. Rotunno et al. (2016) showed that the effective forcing velocity due to the damping is $W_e = 66$ m s$^{-1}$. The radial extension of the domain ($R = 20$ km) is significantly larger than the median radius of maximum wind in tornadoes ($\approx 150$ m, Alexander and Wurman 2008) in order for the linear damping to block the domain top disturbances from being fed back into the vortex traveling along the outer boundary.

We note from Table 1 that all the parameters have a fixed value except for $\Omega$ and $C_d$. The fixed parameters have values that broadly fulfill the requirement of similarity to a supercell (Rotunno 2013). The dimensional parameters $\Omega$ and $\nu$ (kinematic viscosity) can be made nondimensional, obtaining a swirl ratio $S_r = \Omega l_r/W$, related to the system's rotation, and a

Reynolds number Re $= Wl_r/\nu$, representing diffusive effects. The set $S_r$–Re–$C_d$ of nondimensional parameters determines the solution. The combinations of $S_r$–Re–$C_d$ employed in the present work are listed in Table 2. Following the notation of Fiedler (2017), we will refer to the no-slip conditions as $C_d = \infty$ and to the free-slip conditions as $C_d = 0$. We kept Re fixed at 10 000 (by setting $\nu = 24$ m$^2$ s$^{-1}$), and for each of the three $S_r$ values, we performed 16 semislip simulations, with the $C_d$ values reported in Table 2. Along with the semislip cases, we performed simulations with no-slip and free-slip boundary conditions, in order to validate the semislip simulations for very high and very low drag. To put the $C_d$ values of Table 2 into context, we note that, for open sea $C_d \sim 0.0014$ (roughness length $z_0 = 2 \times 10^{-4}$ m), for open flat terrain or grass $C_d \sim 0.005$ ($z_0 = 0.03$ m), for low crops $C_d \sim 0.008$ ($z_0 = 0.1$ m), for high crops $C_d \sim 0.012$ ($z_0 = 0.25$ m), for bushes $C_d \sim 0.017$ ($z_0 = 0.5$ m), for a forest $C_d \sim 0.028$ ($z_0 = 1$ m), while for a city $C_d > 0.05$ ($z_0 > 2$ m) (WMO 2023, chapter 5, p. 220).

The $S_r$–Re parameter space was thoroughly explored in Rotunno et al. (2016) under no-slip boundary conditions. The solution matrices reported in their Figs. 3–5 show that the optimal solutions (vortices producing the maximum pressure drop) occur for $S_r \propto \text{Re}^{-1/3}$. These optimal solutions are vortices undergoing vortex breakdown (Rotunno 2013), and they occur along a diagonal line in the log–log $S_r$–Re parameter space, with single-celled (1-c) vortices below the line, while those above the line present two-celled structures. Using their results, we chose three $S_r$–Re combinations leading to different structures under no-slip conditions (one-celled for Re $= 10 000$–$S_r = 0.005$, very close to vortex breakdown for Re $= 10 000$–$S_r = 0.01$, and two-celled for Re $= 10 000$–$S_r = 0.04$) and studied the effects of semislip boundary conditions on these combinations.

## 3. Governing equations and numerical setup

### a. Governing equations

The dynamics of the flow simulated in Fiedler chambers has usually been described by the axisymmetric, incompressible, constant-density Navier–Stokes equations in a rotating frame of reference in cylindrical coordinates. The assumption of constant density reflects the fact that we focus primarily on the lowest ~1 km AGL, where the constant-density assumption is valid. Unfortunately, the axisymmetric implementation of the numerical model employed for this study [Cloud Model 1 (CM1)] is not compatible with incompressible solvers. Since $(V_{max}/c_s)^2 \ll 1$, where $V_{max}$ indicates the maximum simulated wind speeds and $c_s = 300$ m s$^{-1}$ is the speed of sound in air, the flow is effectively solenoidal ($\nabla \cdot \mathbf{u} = 0$), and it can be considered effectively incompressible (Batchelor 2000, 167–168). The constant-density assumption is obtained by following this

TABLE 1. Parameter settings for the domain shown in Fig. 1.

| $R$ | $Z$ | $z_b$ | $l_z$ | $l_r$ | $z_d$ | $\tau$ | $W$ | $W_e$ | $\Omega$ | $\nu$ | $C_d$ |
|---|---|---|---|---|---|---|---|---|---|---|---|
| 20 km | 15 km | 8 km | 7 km | 3 km | 8 km | 100 s | 80 m s$^{-1}$ | 66 m s$^{-1}$ | Variable | 24 m$^2$ s$^{-1}$ | Variable |

TABLE 2. Combinations of $S_r$–Re–$C_d$ employed in the simulations. The symbols identify the vortex structure: ** for 1-c, × for vb, and — for 2-c.

| Re = 10 000 constant | $S_r = 0.005$ | $S_r = 0.01$ | $S_r = 0.04$ |
|---|---|---|---|
| $C_d = \infty$ | 1-c (**) | 1-c (**) | 2-c (—) |
| $C_d = 0.2$ | ** | vb (×) | — |
| $C_d = 0.1$ | ** | × | — |
| $C_d = 0.08$ | ** | × | — |
| $C_d = 0.07$ | ** | × | — |
| $C_d = 0.06$ | ** | × | — |
| $C_d = 0.05$ | ** | × | — |
| $C_d = 0.04$ | ** | × | — |
| $C_d = 0.035$ | ** | × | — |
| $C_d = 0.03$ | vb (×) | × | — |
| $C_d = 0.025$ | × | × | — |
| $C_d = 0.02$ | × | 2-c (—) | — |
| $C_d = 0.015$ | 2-c (—) | — | — |
| $C_d = 0.01$ | — | — | — |
| $C_d = 0.005$ | — | — | — |
| $C_d = 0.001$ | — | — | — |
| $C_d = 0.0001$ | — | — | — |
| $C_d = 0$ | — | — | — |

rationale: we impose a dry adiabatic base state, with potential temperature $\theta = 300$ K and surface pressure $p_{00} = 1000$ hPa; since this base state is in hydrostatic balance and is kept constant in time, and by exploiting the assumption of solenoidal flow, all the terms referred to the pressure base state give no contribution to the tendencies of the fields integrated in time. Therefore, we can simply consider the perturbation pressure $p'(t) = p(t) - p(0)$, which behaves as a pressure divided by a constant density. We can exploit this property, defining $\phi(t)$ as $p'(t)$ divided by a unit density. The resulting equations are

$$\frac{\partial u}{\partial t} = -u\frac{\partial u}{\partial r} - w\frac{\partial u}{\partial z} - \frac{\partial \phi}{\partial r} + 2\Omega v + \frac{v^2}{r} - \alpha(z)\frac{u}{\tau}$$
$$+ \frac{1}{\rho}\left(\frac{1}{r}\frac{\partial r\tau_{rr}}{\partial r} + \frac{\partial \tau_{rz}}{\partial z} - \frac{\tau_{\theta\theta}}{r}\right), \quad (3a)$$

$$\frac{\partial v}{\partial t} = -u\frac{\partial v}{\partial r} - w\frac{\partial v}{\partial z} - 2\Omega u - \frac{uv}{r} - \alpha(z)\frac{v}{\tau}$$
$$+ \frac{1}{\rho}\left(\frac{1}{r^2}\frac{\partial r^2\tau_{r\theta}}{\partial r} + \frac{\partial \tau_{z\theta}}{\partial z}\right), \quad (3b)$$

$$\frac{\partial w}{\partial t} = -u\frac{\partial w}{\partial r} - w\frac{\partial w}{\partial z} - \frac{\partial \phi}{\partial z} + F(r, z) - \alpha(z)\frac{w}{\tau}$$
$$+ \frac{1}{\rho}\left(\frac{1}{r}\frac{\partial r\tau_{rz}}{\partial r} + \frac{\partial \tau_{zz}}{\partial z}\right), \quad (3c)$$

$$\frac{\partial \phi}{\partial t} = -c_s^2\left[\frac{1}{r}\frac{\partial(ru)}{\partial r} + \frac{\partial w}{\partial z}\right], \quad (3d)$$

where $u$, $v$, and $w$ are the radial, tangential (azimuthal), and vertical velocity components, respectively, $\tau_{ij}$ is the stress tensor, and $\alpha(z)$ is the damping function.

We employ the updraft forcing $F(r, z)$ defined in Nolan (2005),

$$F(r, z) = \begin{cases} F_{\max}\cos\left(\frac{\pi}{2}\chi\right) & \text{for } \chi < 1 \\ 0 & \text{for } \chi \geq 1 \end{cases}, \quad (4)$$

where

$$\chi = \left[\frac{(z - z_b)^2}{l_z^2} + \frac{r^2}{l_r^2}\right]^{1/2} \quad (5)$$

is a normalized distance from the center of the ellipse. The formulation of $F_{\max}$ can be obtained by substituting Eq. (4) in Eq. (2): $F_{\max} = W^2\pi/8l_z$.

Finally, the linear damping is governed by the damping function $\alpha(z)$, which determines the distance over which full damping with time constant $\tau$ is achieved,

$$\alpha(z) = \begin{cases} \frac{1}{2}\left[1 - \cos\left(\pi\frac{z - z_d}{Z - z_d}\right)\right] & \text{for } z > z_d \\ 0 & \text{for } z \leq z_d \end{cases}. \quad (6)$$

### b. Numerical implementation and model setup

The numerical model used in this study is CM1 (Bryan and Fritsch 2002) in its 19.10 release. CM1 is a nonhydrostatic numerical model designed mainly for idealized simulations. The numerical scheme used to integrate in time equations [(3a)–(3d)] is the third-order Runge–Kutta scheme described in Wicker and Skamarock (2002), which uses Klemp–Wilhelmson (Klemp and Wilhelmson 1978) split-time steps for acoustic modes, with explicit treatment of the acoustic terms in both vertical and horizontal directions. A weak artificial damping of acoustic waves is introduced to improve the stability of the split-time integration scheme, following the three-dimensional divergence damper of Skamarock and Klemp (1992). An adaptive time step is used to maintain numerical stability. We employ fifth-order advection schemes in both vertical and horizontal directions for scalars and vectors. The advection of velocities is performed using a fifth-order weighted essentially nonoscillatory (WENO) scheme on the final Runge–Kutta step (Borges et al. 2008). No turbulence model is employed in the present work. Along with the adiabatic base state for pressure, we employed a zero-wind initial condition.

The equations are solved on a staggered grid with 276 radial grid points and 266 vertical grid points. The radial grid spacing is 5 m for $r < 1$ km (i.e., the first 200 radial grid cells), and it gradually increases to 495 m at $r = 20$ km (for the remaining 76 grid cells). The stretching in the radial direction is performed following Wilhelmson and Chen (1982), defining a transformation between the actual radius $r$ and the radius $r'$ in the coordinate system with constant radial grid spacing:

$$\begin{cases} r_{200+i} = 1000 + (C_1 + C_2 r'_i)r'_i \\ r'_i = i\Delta r' \end{cases} \text{ for } i = 1, 2, ..., 76, \quad (7)$$

where $\Delta r' = 250$ m, $C_1 = 6.9 \times 10^{-3}$, and $C_2 = 5.2 \times 10^{-5}$ m$^{-1}$. The vertical grid spacing is 5 m for $z < 1$ km, and the grid stretching in the remaining 66 cells is performed using a

geometric progression, limited to a maximum grid spacing of 495 m (reached at ~6 km):

$$\begin{cases} \Delta z_{200+i+1} = s \times \Delta z_{200+i} & \text{if } \Delta z_{200+i} \le 495 \text{ m} \\ \Delta z_{200+i+1} = 495 \text{ m} & \text{if } \Delta z_{200+i} = 495 \text{ m} \end{cases}, \quad (8)$$

where $s = 1.0989$ is the grid stretch factor.

## 4. Results

In the present work, steady-state solutions are the objects of the investigation. The nature of the steadiness is related to the nature of the vortex: one-celled vortices achieve an asymptotic steady state (the time derivatives of the solution tend to zero as $t \to \infty$), while transitional and two-celled vortices reach a statistically steady state (given a time window, the time derivatives of the solution averaged over the window tend to zero as $t \to \infty$). Consequently, every simulation has been carried out until a stationary state was reached. Moreover, all data and plots represent an average over 10 000 s (10 model outputs).

For simplicity, we will refer to $\phi$ as pressure or pressure drop in the remainder of this work.

### a. Preservation of the potential vortex structure under semislip conditions

Since one of the goals of the present work is to study how the boundary layer of a potential vortex changes when employing semislip conditions instead of no-slip ones, we must first make sure that the potential vortex structure of the solutions is preserved under semislip conditions. Since the defining property of a potential vortex is that the angular momentum per unit mass (hereafter simply angular momentum) $\Gamma = rv$ is radially constant, we analyzed the radial profile of $\Gamma$ above the boundary layer. All the simulations present a region, roughly delimited by $1 \lesssim r \lesssim 2$ km and $1 \lesssim z \lesssim 2$ km, where $\Gamma$ is radially constant, hence where the solution displays a potential vortex structure. An example of this feature is presented in Fig. 2, showing the radial profile of $\Gamma/\Gamma_\infty$ for $S_r =$ 0.005, where $\Gamma_\infty$ is the outer angular momentum, i.e., the maximum value of $\Gamma$ within the potential vortex region. The profile is sampled at $z = 1.5$ km under no-slip conditions as well as semislip conditions for various values of $C_d$. The angular momentum is approximately constant in the region $1 \lesssim r \lesssim 2$ km, with variations of less than 1% of $\Gamma_\infty$. For $r > 2$ km, $\Gamma$ slowly decreases, and the assumption of a potential vortex becomes less accurate.

### b. Effects on the potential vortex boundary layer

We study the boundary layers of potential vortices under semislip conditions varying $C_d$, and we compare the results with the ones of Burggraf et al. (1971), who studied the potential vortex boundary layer developing on a disc of finite radius under no-slip conditions. According to that study, the boundary layer presents a two-tiered structure, which can be appreciated by plotting the $-ur/\Gamma_\infty$ and $vr/\Gamma_\infty$ vertical profiles sampled at various radii. In tornado dynamics literature, the upper tier is referred to as the "inertial layer," while the lower
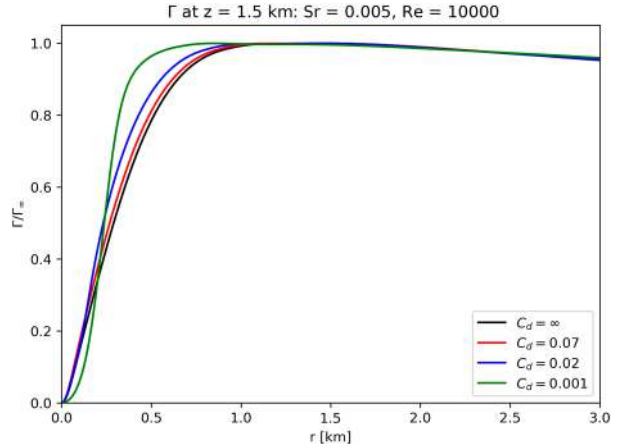


FIG. 2. Radial profiles of angular momentum $\Gamma$ divided by $\Gamma_\infty$ for $S_r = 0.005$ sampled at $z = 1.5$ km under no-slip conditions (black) and semislip conditions with $C_d = 0.07$ (red), $C_d = 0.02$ (blue), and $C_d = 0.001$ (green).

as the "frictional layer." The authors employed nondimensional coordinates in their work: $a$ is the finite-disc radius, $\nu$ is the kinematic viscosity, and $\xi = -\ln(r/a)$; hence, $\xi$ increases for decreasing radius. Figure 3 shows that the tiers are delimited by the maximum in $-ur/\Gamma_\infty$, with $-ur/\Gamma_\infty$ increasing with height in the frictional layer and decreasing in the inertial layer. The maximum in $-ur/\Gamma_\infty$ becomes larger and shifts downward as the radius decreases. As a result, the frictional layer becomes vanishingly thinner and finally disappears in the limit $r \to 0$, leaving only the inertial layer. The angular momentum $rv$ increases monotonically with height from zero toward the outer value $\Gamma_\infty$, and the increase is larger for smaller radii. A conceptual model of the two-tiered boundary layer with respect to the structure of the vortex is shown in Fig. 4.

The results for a sequence of semislip simulations are presented in Fig. 5 for $C_d = 0.2$ (black lines), $C_d = 0.05$ (red lines), $C_d = 0.01$ (blue lines), $C_d = 0.005$ (magenta lines), and $C_d = 0.001$ (green lines). The left column (Figs. 5a,d) shows the vertical profiles sampled at $r = 1.75$ km for $S_r = 0.005$, the middle column (Figs. 5b,e) for $S_r = 0.01$, and the right column (Figs. 5c,f) for $S_r = 0.04$. The top row displays the profiles of $-ur/\Gamma_\infty$, and the bottom row displays the profiles of $vr/\Gamma_\infty$.

We preliminarily note that the swirl ratio plays a part in determining the structure of the potential vortex boundary layer. Scanning Fig. 5 from left to right while keeping $C_d$ fixed, it is evident how for larger $S_r$ values the frictional layer is thinner, and $rv$ reaches the outer value of angular momentum $\Gamma_\infty$ at a lower height.

Focusing on the $-ur/\Gamma_\infty$ profiles, the two-tier structure clearly emerges, demonstrating the development of a potential vortex boundary layer for the semislip simulations. We can appreciate the role of the drag coefficient by noticing the differences in the vertical profiles for different $C_d$ values, while keeping $S_r$ constant (Figs. 5a–c). While the profiles in Fig. 3 start from zero for $z = 0$, as a consequence of the no-slip conditions, the semislip simulations present nonzero wind
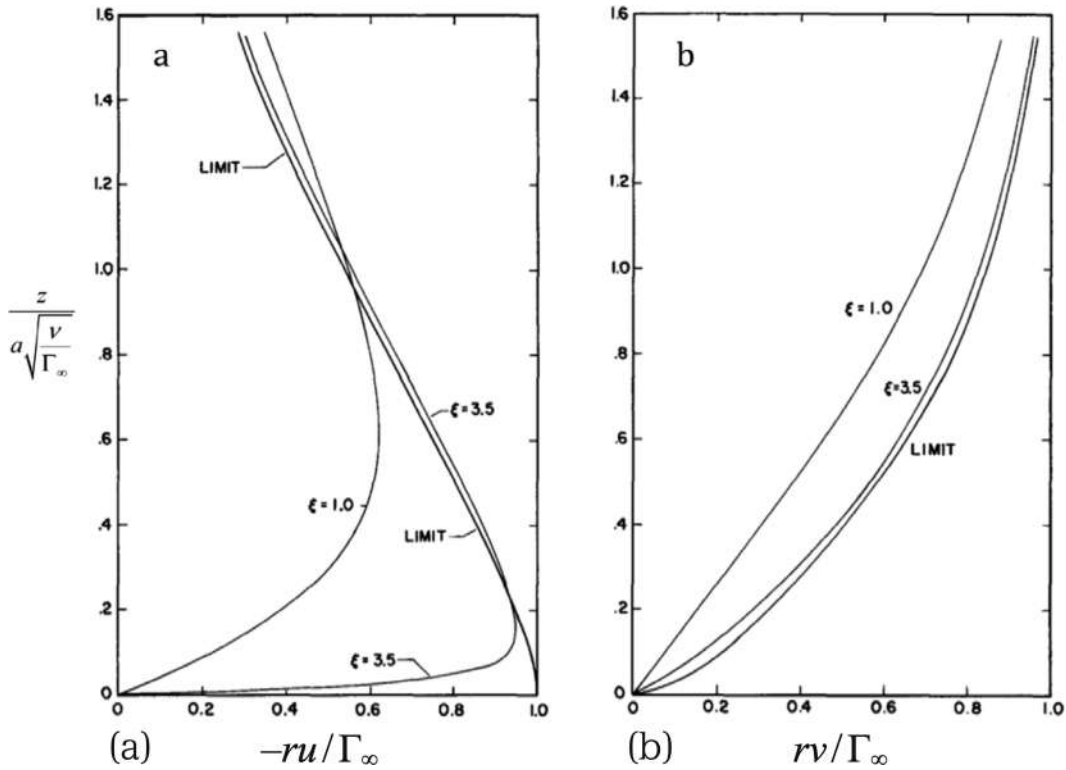
FIG. 3. Boundary layer profiles of (a) $-ur/\Gamma_\infty$ and (b) $vr/\Gamma_\infty$ under no-slip conditions for a potential vortex at different radii, along with the limit $r \to 0$ (for $\xi \to \infty$). Figure adapted from Burggraf et al. (1971).

speed at the lowest grid point. Moreover, a reduction in $C_d$ results in an increase in ground wind speed; hence, the profiles start from larger values. A decrease in $C_d$ appears to shift the profile downward, reducing the thickness of the lower tier of the boundary layer. There is also a small decrease in the



FIG. 4. Conceptual model of the two-tiered boundary layer under no-slip conditions. Figure from Bluestein (2013, chapter 6).

magnitude of the maximum of $-ur/\Gamma_\infty$. Examining the $vr/\Gamma_\infty$ profiles (Figs. 5d–f), we notice that for lower $C_d$, the asymptotic value $\Gamma_\infty$ is reached at a lower height due to the profiles starting at larger values.

Since for lower $C_d$ values, the lower tier of the boundary layer becomes thinner, we expect to find a critical value of drag coefficient for which the frictional layer vanishes and only the inertial layer is present. Despite the thickness of the frictional layer being smaller for larger values of $S_r$, we found $C_d = 0.001$ to be the first of the $C_d$ values employed for which the frictional layer is not present for all three $S_r$ values explored (Fig. 5). The $C_d = 0.005$ is the smallest value for which a two-tiered structure is present; hence, the critical $C_d$ value must be included in the range $0.001 \leq C_d < 0.005$. Once the two-tiered structure is lost, the maximum value of $-ur/\Gamma_\infty$ is located at the lowest grid point, and $-ur/\Gamma_\infty$ decreases with height. Moreover, Fig. 5 shows that the magnitude of the maximum is significantly smaller than that for the two-tiered profiles, indicating a substantial weakening of the radial inflow. The profile of $vr/\Gamma_\infty$ shows increased vertical invariance, with $vr/\Gamma_\infty$ starting at $0.9\Gamma_\infty$ and quickly approaching $\Gamma_\infty$ with height. This behavior explains how solutions under semislip conditions reconcile with free-slip ones as $C_d \to 0$. Free-slip solutions, lacking a frictional lower boundary, cannot develop a boundary layer; hence, they display significant vertical invariance. Since the presence of a radial inflow is related to the action of surface friction (Rotunno 2013), the inflow is not present in free-slip simulations.
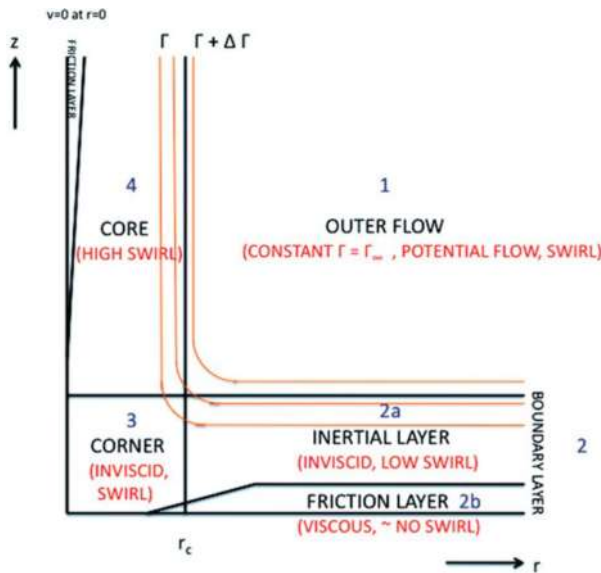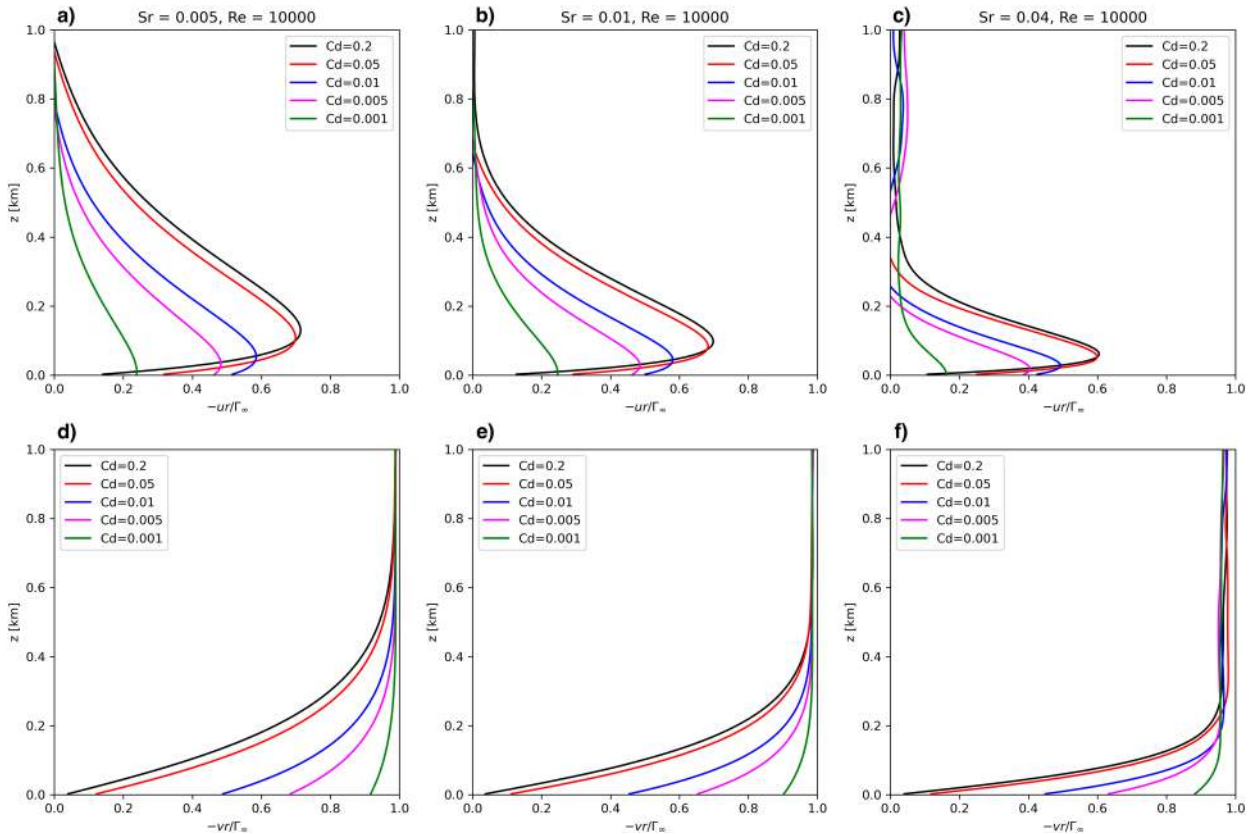
FIG. 5. Vertical profiles of (top) $-ur/\Gamma_\infty$ and (bottom) $vr/\Gamma_\infty$ sampled at $r = 1.75$ km for (a),(d) $S_r = 0.005$; (b),(e) $S_r = 0.01$; and (c),(f) $S_r = 0.04$. The profiles are displayed for $C_d = 0.2$ (black), $C_d = 0.05$ (red), $C_d = 0.01$ (blue), $C_d = 0.005$ (magenta), and $C_d = 0.001$ (green).

The vertical profiles of $-ur/\Gamma_\infty$ and $vr/\Gamma_\infty$ for the semislip simulations display the same behavior with decreasing radii as previously found for no-slip conditions. Figure 6 provides an example, showing the vertical profiles for $S_r = 0.005$ and $C_d = 0.05$, sampled at $r = 1$ km (black), $r = 2$ km (red), and $r = 4$ km (blue). The maximum of $-ur/\Gamma_\infty$ (Fig. 6a) increases and shifts downward for decreasing radius. Clearly, the limit $r \rightarrow 0$ is not applicable in the present case, as we have seen in Fig. 2 that the
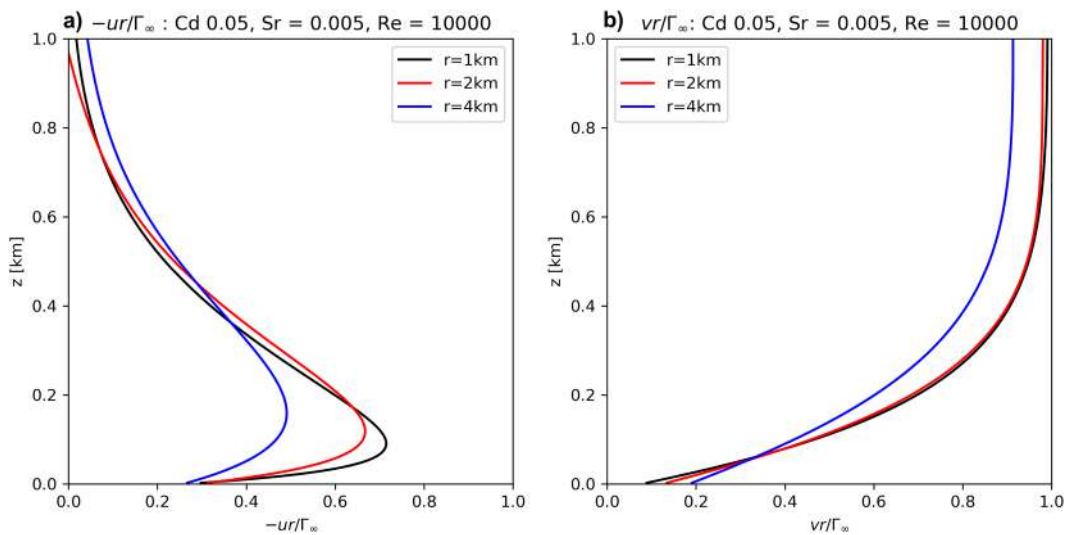


FIG. 6. Vertical profiles of (a) $-ur/\Gamma_\infty$ and (b) $vr/\Gamma_\infty$ sampled at $r = 1$ km (black), $r = 2$ km (red), and $r = 4$ km (blue) for $S_r = 0.005$, $C_d = 0.05$.

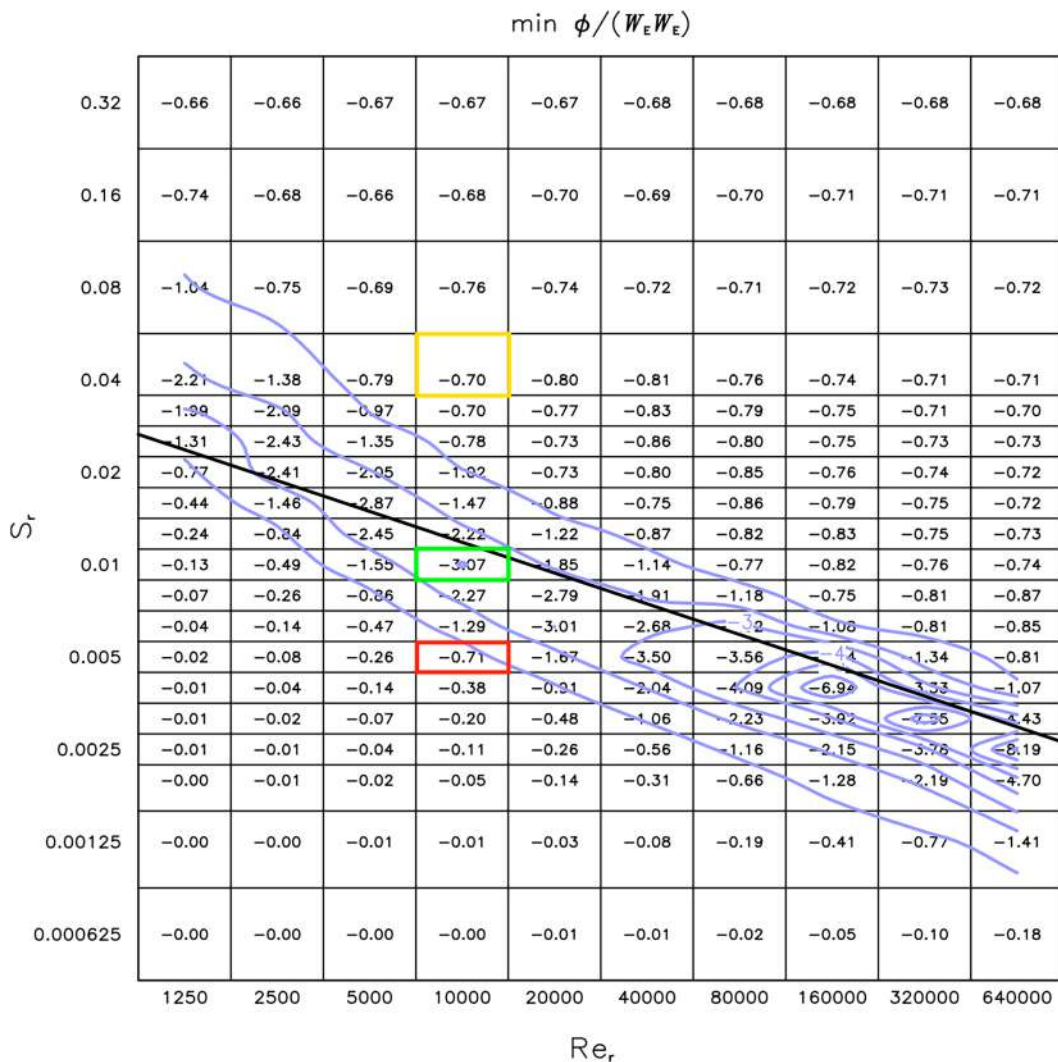$$\min\ \phi/(W_{\varepsilon}W_{\varepsilon})$$



FIG. 7. Solution matrix in the $S_r$–Re space for the maximum pressure drop (minimum $\phi$) normalized by $W_e^2$ for no-slip simulations. Optimal vortices tend to occur along a diagonal line, representing a proportionality of the kind $S_r \propto \mathrm{Re}^{-1/3}$. The colored boxes identify the $S_r$–Re combinations employed in the present work. Adapted from Rotunno et al. (2016).

defining property $\Gamma = \Gamma_\infty$ of the potential vortex is true only for $r \gtrsim 1$ km. Indeed, instead of vanishing for $r \to 0$, the lower tier of the boundary layer has roughly the same thickness in the range $0.25 < r < 1$ km. The $vr/\Gamma_\infty$ profiles (Fig. 6b) likewise show the same behavior for decreasing radii as in the no-slip case, with $vr$ approaching $\Gamma_\infty$ at lower heights for smaller radii. Figure 6b confirms the findings of Fig. 2, as the profiles sampled at $r = 1$ km and $r = 2$ km show very similar asymptotic values, while the one sampled at $r = 4$ km tends to an asymptotic value slightly smaller than $\Gamma_\infty$.

### c. The role of $C_d$ on the structure of the vortex

As previously mentioned, the structure of a potential vortex with no-slip boundary conditions depends on two parameters: the swirl ratio and the Reynolds number. This dependence

has been thoroughly explored in Rotunno et al. (2016). According to these authors, the combination $S_r \propto \mathrm{Re}^{-1/3}$ yields an optimal vortex, defined as the combination for which the greatest pressure drop is simulated. They argued that the constant of proportionality may be dependent on the specific details of the simulation (such as domain size, upper-layer damping, etc.), but the proportionality should be universal. On a log–log $S_r$–Re space, the proportionality appears as a diagonal line, with single-celled vortices below the line, whereas those above are two-celled solutions (Fig. 7, where the colored boxes represent the $S_r$–Re combinations chosen for this study). In the present work, the use of semislip conditions introduces another parameter, the drag coefficient $C_d$. It is therefore natural to ask if this additional parameter plays a role in defining the nature of a vortex. We investigate the effects of semislip boundary conditions on the structure of the
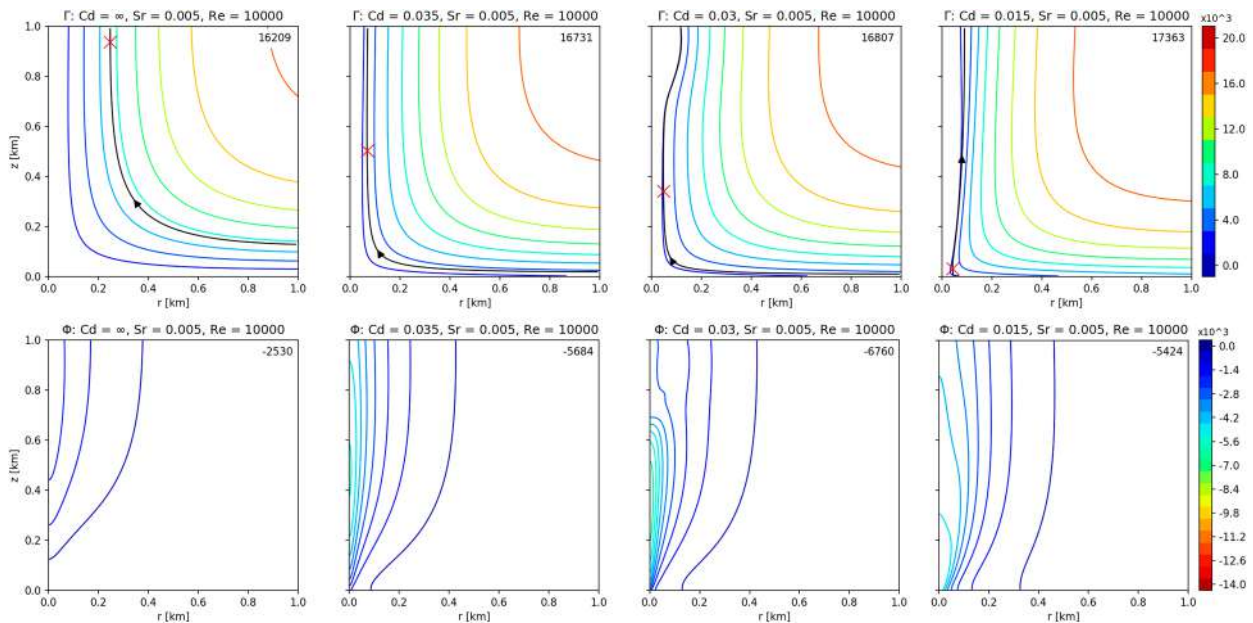
FIG. 8. (top) Angular momentum $\Gamma$ (m$^2$ s$^{-1}$) and (bottom) pressure $\phi$ (Pa m$^3$ kg$^{-1}$) contour lines in the 1 km × 1 km window from the origin for $S_r = 0.005$, Re = 10 000. (from left to right) The boundary conditions employed are no slip ($C_d = \infty$) and semislip with $C_d = 0.035$, $C_d = 0.03$, and $C_d = 0.015$. The red × is the position of the maximum tangential velocity, and the solid black line is the streamline referring to that position. The value in the top-right corner of the figure panels is a maximum for $\Gamma$ and a minimum for $\phi$.

vortex examining the solutions for the $C_d$ values listed in Table 2. It can be seen from Fig. 7 that the three $S_r$–Re combinations represent different positions with respect to the $S_r \propto \text{Re}^{-1/3}$ diagonal line: the choice of parameters allows us to study the role of $C_d$ for vortices with different structures under no-slip conditions.

### 1) THE EFFECT OF $C_d$ ON THE STRUCTURE OF THE VORTEX FOR $S_r = 0.005$

To study the role of $C_d$ in determining the structure of the vortex, we examined the angular momentum and the pressure (Fig. 8), along with the tangential, radial, and vertical wind components (Fig. 9). Scanning Figs. 8 and 9 from left to right, we can visualize these fields for $S_r = 0.005$ and decreasing friction, from no-slip conditions ($C_d = \infty$) to $C_d = 0.035$, $C_d = 0.03$, and $C_d = 0.015$. All the fields are plotted in a 1 km × 1 km window with the origin as the bottom-left corner.

Under no-slip conditions, the vortex exhibits a single-celled structure, as expected considering the red box in Fig. 7 lies firmly below the diagonal line. The single-cell structure is evident by looking at the vertical wind speed, which shows a central updraft across the windowed in view of the domain (Fig. 9). We notice how the no-slip condition results in weak fields close to the surface. In particular, the updraft and the pressure drop show near-zero values in the proximity to the origin and gradually increase in magnitude with height.

Moving to semislip conditions with $C_d = 0.035$, the vortex tightens and intensifies considerably while retaining a one-celled structure. The $\Gamma$ contours are closer to the surface and the origin, indicating that parcels with larger angular momentum are

advected by the inflow toward the origin, and then deviate upward in a more confined region of the domain, feeding the updraft. We can better visualize this behavior by plotting the streamline (black solid line in the $\Gamma$ plot) passing from the point of maximum tangential velocity (red ×), which describes a radial movement toward the origin occurring closer to the surface, followed by a sharp deviation upward, in contrast to the smoother curve described by the no-slip streamline. The inflow is therefore able to penetrate further in the corner flow region (toward the origin) before deviating, causing gradients to intensify. Past studies have shown the same behavior as the corner flow swirl ratio $S_c$ approaches the critical value (Lewellen et al. 2000; Lewellen and Lewellen 2007a,b). The discussion and computation of $S_c$ for the present simulations are provided in section 4c(4). The upward deviation of the inflow is a consequence of mass conservation: due to the axisymmetric nature of the simulations, a radial inflow would collide with the inflow coming from the opposite direction with respect to the origin, and the only mass-conserving possibility is to deviate upward. This is numerically reproduced by imposing an impermeable $r = 0$ boundary. The transition from the relatively broad no-slip structure to the intense swirling motion adjacent to the vertical axis displayed for $C_d = 0.035$ illustrates the tightening of the vortex for a decreasing drag coefficient. In particular, max($v$) is reached around $r \approx 0.3$ km in the no-slip case and around $r \approx 0.1$ km for $C_d = 0.035$. It is worth pointing out the intense radial gradient of $v$ develops as a result of the tightening. The intensification of the vortex is significant: max($v$) increases from 29.29 to 41.83 m s$^{-1}$, max($w$) increases from 59.42 to 78.65 m s$^{-1}$, and min($\phi$) deepens to more than double the no-slip pressure drop, going from $-2530$ to $-5684$ (Pa m$^3$ kg$^{-1}$).
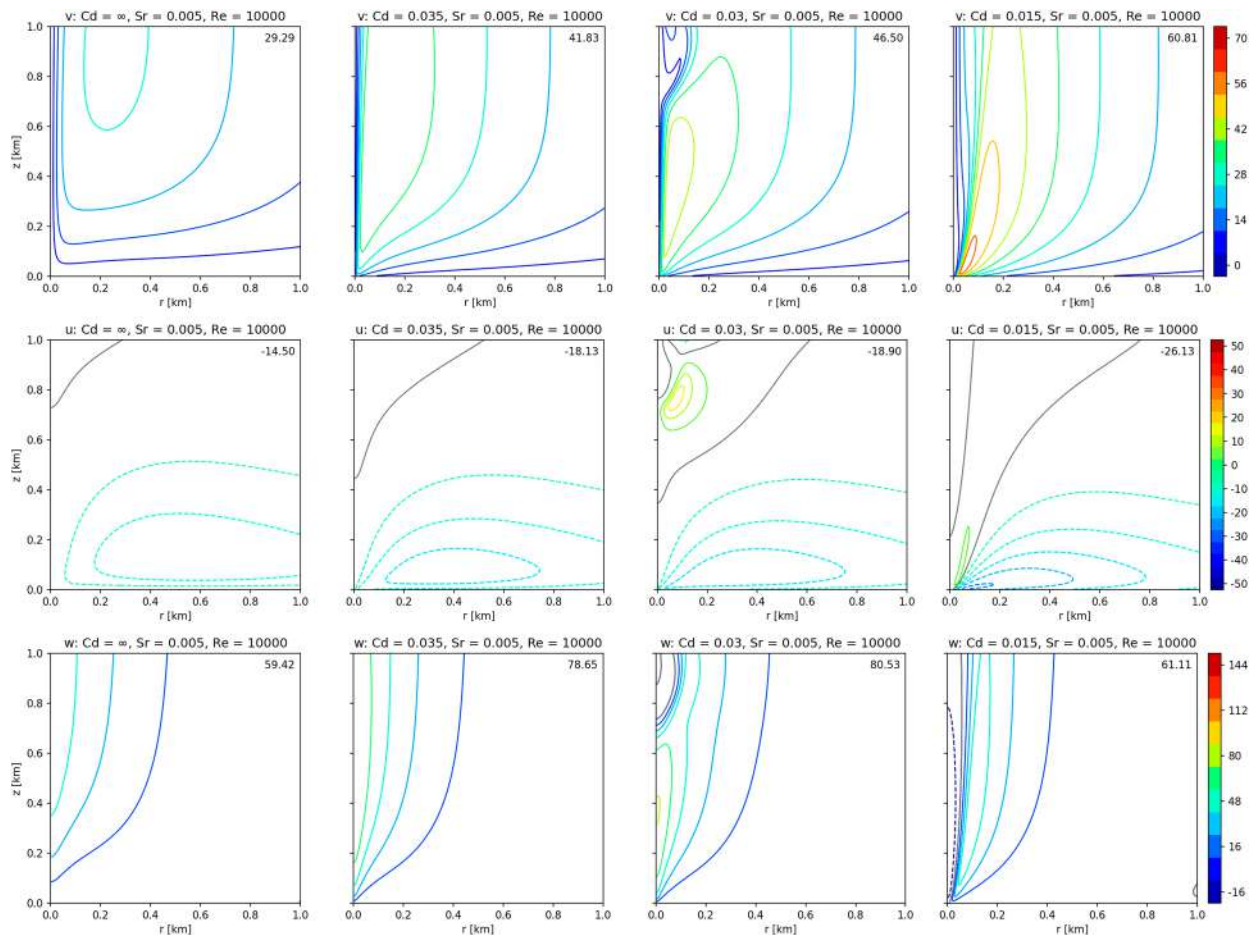
FIG. 9. As in Fig. 8, but for (top) tangential $v$, (middle) radial $u$, and (bottom) vertical velocity $w$ (m s$^{-1}$). The zero contour is in gray for $u$ and $w$. Solid lines represent positive contours; dashed lines represent negative contours. The value in the top-right corner of the figure panels is a maximum for $v$ and $w$, whereas for $u$, it is a minimum.

A feature that emerges for $C_d = 0.035$ is an intensification of the tornado within the corner flow region (near the origin). While this is true for all the fields, it is particularly evident for $w$ and $\phi$, which show significant values close to the origin, in contrast to the small values of the no-slip case. This phenomenon is a consequence of the change in lower boundary conditions from no-slip to semislip, which allows the wind speed to have nonzero values at the surface, heightening the importance of the region in proximity to the origin. This region represents the near-surface, central portion of the tornado and is therefore important in determining the impact on buildings and structures. Figure 9 shows that the shift to semislip conditions causes an intensification of the inflow, which moves toward the origin and becomes narrower. It is worth noting that we chose to display the $C_d = 0.035$ case to better appreciate the differences between the no-slip and semislip cases, but these occur gradually as we decrease the value of $C_d$ employed in the simulations.

In clear contrast with the progressive tightening of the vortex for decreasing drag coefficient, a slight reduction in $C_d$ from $C_d = 0.035$ to $C_d = 0.03$ leads to an abrupt modification

of the vortex structure. Examining the vertical velocity, we note that the central updraft is suddenly forced to deviate outward at around $z \approx 0.7$ km by a central downdraft coming from above (Fig. 9). The deviation outward is evident in the radial velocity field, with a radial outflow. These features indicate that the vortex undergoes a breakdown for $C_d = 0.03$. The abrupt expansion of the vortex is visible in the $v$ field as an area of reduced tangential velocity above $z \approx 0.7$ km and in the $\Gamma$ field as a bulge of low angular momentum. Interestingly, we observe that the streamline passing through max($v$) describes an almost vertical flow from $z = 0.2$ to 0.6 km, followed by a deviation around the interface between the one-celled vortex below and the two-celled one above. The solution arising from the present combination of parameters displays the structure found in "optimal vortices," with the coexistence of a two-celled vortex suspended above a single-celled one (Rotunno 2013; Rotunno et al. 2016; Fiedler and Rotunno 1986; Fiedler 2009). In fact, the maximum pressure drop is simulated for the next lower value of $C_d$, namely, $C_d = 0.025$. The vortex is considered optimal in the sense that it is the vortex for which the tangential velocity in the one-celled
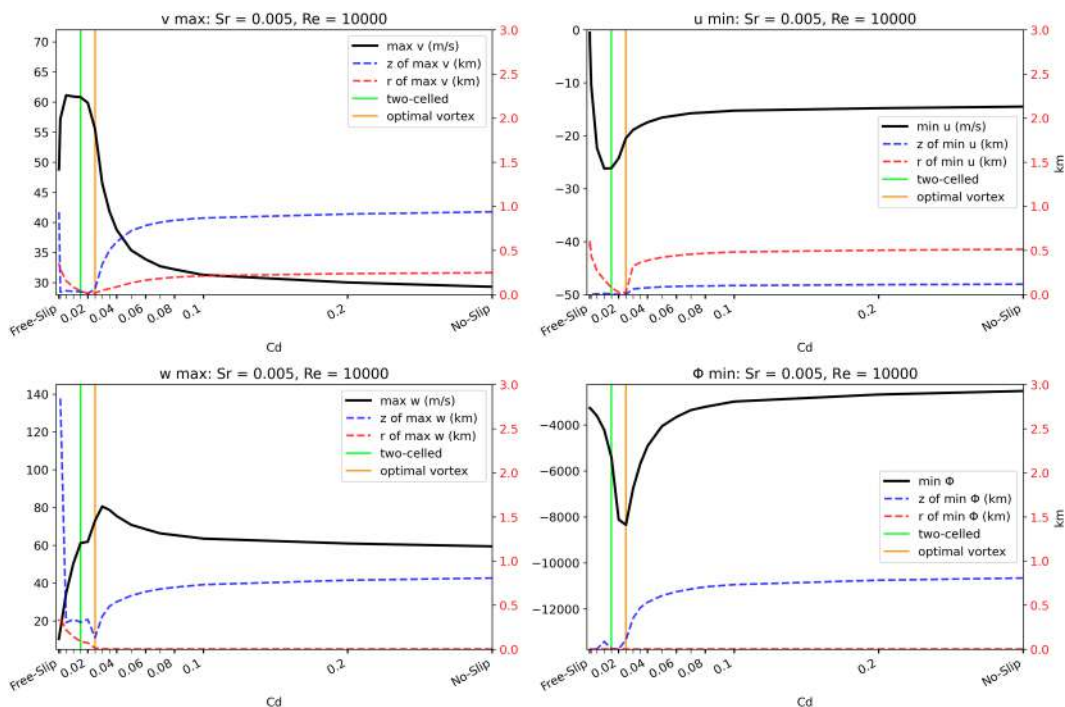
FIG. 10. Extrema of $v$, $u$, $w$ (m s$^{-1}$), $\phi$ (Pa m$^3$ kg$^{-1}$) (black solid lines), and their radial $r$ (dashed red lines) and vertical $z$ (dashed blue lines) positions (km) for $S_r = 0.005$, Re = 10 000, and boundary conditions ranging from no slip to free slip. The vertical green line identifies the largest $C_d$ for which the vortex is two-celled; the vertical orange line identifies the optimal vortex.

portion (influenced by the boundary layer) has the maximum amplification with respect to the core velocity aloft $v_{\text{aloft}}$, i.e., downstream of the vortex breakdown ($v_{\text{aloft}}$ is determined by the buoyancy of the updraft). Rotunno (2013) showed that $v_{\text{max}} \approx 5/3 \, v_{\text{aloft}}$ under the assumption of no-slip conditions; this proportionality holds for the optimal semislip solutions of this work. The vortex exhibits further intensification compared to the $C_d = 0.035$ case, in particular, close to the origin.

A further decrease in the drag coefficient leads to the descent of the interface between the one-celled and two-celled vortices. For $C_d = 0.015$, the interface reaches the surface, and the vortex displays a complete two-celled structure. In the $w$ field, the downdraft extends all the way to the surface, surrounded by a weakened updraft (bottom-right corner of Fig. 9). After the transition to a two-celled structure, the pressure drop weakens considerably (bottom-right corner of Fig. 8), while the inflow strengthens further (central-right edge of Fig. 9). The vortex exhibits a significantly stronger swirling motion localized in proximity to the origin (top-right corner of Fig. 9). Interestingly, the streamline passing through max($v$) describes a radial motion that follows the inflow at the lowest grid point, followed by an abrupt deviation upward (top-right corner of Fig. 8).

To further assess the role of $C_d$ on the structure of the vortex, we plot the extrema of $v$, $u$, $w$, $\phi$, and their positions for $S_r = 0.005$ and for all the $C_d$ values employed in this work (Fig. 10). The search for the extrema is carried out in a 3 km × 3 km window starting from the origin. The most striking

feature of Fig. 10 is that all the fields display a clear peak in the magnitude of the extrema. The peaks occur for $C_d$ values between the vortex breakdown ($C_d = 0.03$) and the two-celled vortex ($C_d = 0.015$). Figure 10 highlights all the structural changes brought by a decrease in the $C_d$ value employed:

1) Tightening and intensification of the vortex, increased importance of the origin (from no-slip up to the transition to a two-celled structure at $C_d = 0.015$): The tightening is clear by the progressive shift of the extrema of $v$ and $u$ toward smaller radii (dashed red line). The gradual decrease in the height of the extrema (dashed blue line) illustrates the evolution of the area close to the origin from a broad stagnant area to a region of intense swirling motion and strong gradients.

2) Vortex breakdown ($C_d = 0.03$) and transition to a two-celled structure ($C_d = 0.015$): The radial position of the maximum updraft is zero (central updraft) up to $C_d = 0.03$, and then it shifts to larger radii for lower drag coefficient (updraft surrounding a central downdraft). The decrease in the radial position of max($v$) and min($u$) is abruptly reverted for $C_d$ from 0.025 to 0.015, pointing out the transition to a two-celled structure.

3) Widening of the two-celled vortex for decreasing drag coefficient ($C_d \leq 0.025$): As illustrated by the increase in the radial position of the extrema of $v$, $u$, and $w$, the vortex widens for decreasing $C_d$ after achieving a two-celled structure.

4) Tendency to free-slip solution for $C_d \rightarrow 0$: $u$ and $w$ tend to zero after the peak as the solutions converge to the
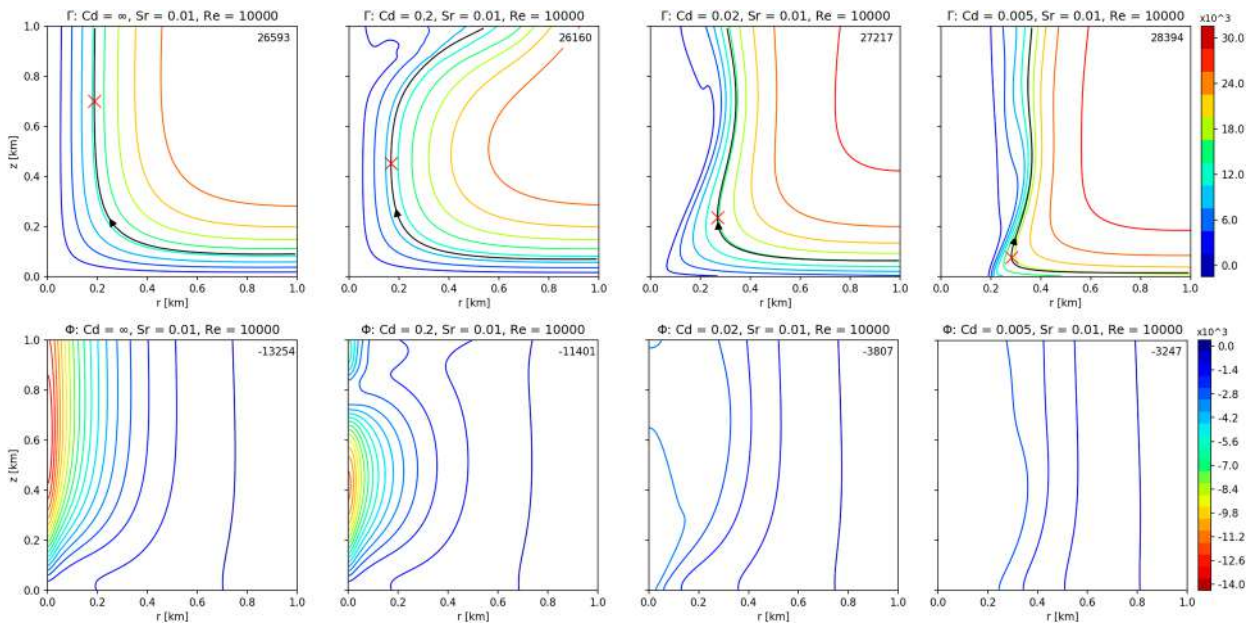
FIG. 11. As in Fig. 8, but for $S_r = 0.01$. (from left to right) The boundary conditions employed are no slip ($C_d = \infty$) and semislip with $C_d = 0.2$, $C_d = 0.02$, and $C_d = 0.005$.

free-slip case for $C_d \to 0$. Free-slip solutions are characterized by a complete lack of inflow and reduced updraft at low levels.

The sharp increase in the height of the extrema of $v$ under free-slip conditions is a consequence of the vertical invariance of free-slip solutions, which are almost constant with height; hence, the vertical position of the extrema loses significance (in fact, the maximum of $v$ is reached outside of the 3 km $\times$ 3 km window that we explored, at around 3.5 km, yet the difference with the maximum within the window is less than 0.1% of the absolute maximum of $v$). For $w$, the sharp increase of $z$ reflects the lack of an updraft at low levels for semislip solutions; therefore, the updraft is only present at higher levels, in correspondence with the area where the forcing is active.

A feature worth pointing out is that the maximum tangential wind speed is found at very low levels for $C_d < 0.03$. In particular, for $C_d = 0.02$, max($v$) is found as low as $z = 12.5$ m. This finding is in agreement with recent Doppler on Wheels measurements (Kosiba and Wurman 2023), which observed max($v$) for $z < 15$ m.

It is remarkable how the transitions of the vortex structure for decreasing drag coefficient are in complete analogy to the structural evolution observed under no-slip conditions for an increase in swirl ratio. These findings demonstrate the crucial role of the drag coefficient in determining the structure of the vortex, and they suggest that the $S_r$–Re parameter space should be extended to a three-dimensional space that includes the drag coefficient. A possible consequence of this result is that the potential vortex line, described in Rotunno et al. (2016), might be a slanted surface in the three-dimensional parameter space.

It is worth pointing out that Fig. 10 shows how the maximum tangential wind speed simulated under semislip conditions is

significantly larger than the ones simulated under no-slip and free-slip conditions, the two conditions more commonly used in idealized axisymmetric simulations of tornadoes.

2) THE EFFECT OF $C_d$ ON THE STRUCTURE OF THE VORTEX FOR $S_r = 0.01$

In light of the results of the semislip simulations for $S_r = 0.005$, it is natural to expect that for $S_r = 0.01$, the vortex undergoes breakdown for much larger values of the drag coefficient, as the vortex is very close to the transition under no-slip boundary conditions. In fact, Fig. 7 shows that the combination $S_r = 0.01 - $Re = 10 000 (green rectangle) sits right below the line indicating the optimal vortex (and, therefore, the vortex breakdown).

The analysis for $S_r = 0.01$ is carried out using the same approach of Figs. 8 and 9 but displays the simulations for different $C_d$ values: $C_d = 0.2$, 0.02, and 0.005 (Figs. 11 and 12). These specific values reflect the transitions in vortex structure across the $C_d$ range for $S_r = 0.01$. Consistent with the results for $S_r = 0.005$, a decrease in friction from no-slip to semislip conditions triggers a vortex breakdown event. However, the closeness of the no-slip case to the optimal vortex line in the $S_r - $Re parameter space results in the occurrence of the vortex breakdown already in the simulation for the largest value of $C_d$ explored in this study, $C_d = 0.2$. For the same reason, the no-slip solution is a very tight and intense vortex displaying a very strong vertical jet, with a maximum updraft speed of $\approx$140 m s$^{-1}$. As for the previous case, the vortex breakdown is evident by the bulge of low $\Gamma$ and low $v$ from around $z \approx 0.8$ km, in correspondence with a radial outflow. The downdraft is less evident compared to the previous case, as it descends diagonally rather than centrally, but it still results in a sudden interruption of the vertical updraft jet. It is
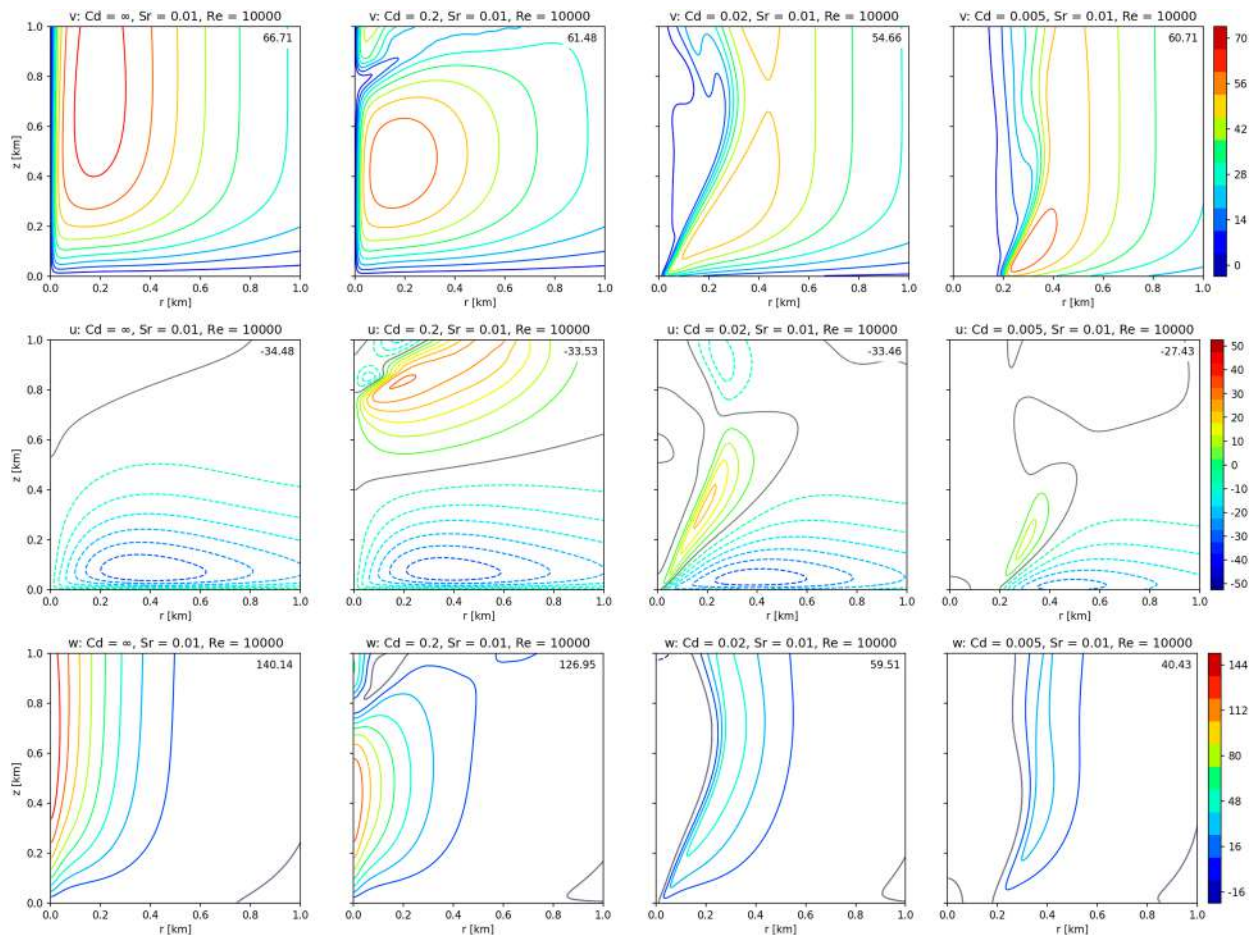
FIG. 12. As in Fig. 9, but for $S_r = 0.01$. (from left to right) The boundary conditions employed are no slip ($C_d = \infty$) and semislip with $C_d = 0.2$, $C_d = 0.02$, and $C_d = 0.005$.

noteworthy that there is no evidence of a peak in intensity of the vortex but rather a slight weakening going from no-slip to semislip conditions with $C_d = 0.2$. Considering that the simulation for the highest $C_d$ already represents a vortex breakdown event, and how close the corresponding no-slip case is to transition, the optimal vortex may occur for higher values of $C_d$ than those explored in this study. A continuation of this work, including more semislip simulations for vortices close to transition, might shed some light on this topic.

Similarly to the previous case, the breakdown progresses downward for decreasing friction, and the downdraft reaches the surface for $C_d = 0.02$, marking the transition to a two-celled vortex, which is met with a significant decrease in the pressure drop and the updraft intensity. As for $S_r = 0.005$, a decrease in $C_d$ leads to increased importance of the area in proximity of the origin. The simulation for $C_d = 0.02$ illustrates this phenomenon, with large values of tangential velocity close to the origin.

A further decrease in friction leads to the expansion of the vortex. For $C_d = 0.005$, the $\Gamma$, $v$, and $u$ fields show negligible values from $r = 0$ up to $r \approx 0.2$ km, in the inner part of the two-celled vortex, characterized by a weak central downdraft.

Moreover, there is a clear tendency toward the free-slip solution, indicated by the enhanced vertical invariance of all the fields.

Figure 13 shows the extrema of the fields and their positions for all the $C_d$ values. As previously mentioned, there is no intensity peak: since for the largest value of drag coefficient, the vortex undergoes breakdown, an intensity peak may be present for larger values of $C_d$ than the ones explored here. There is limited variation with $C_d$ in the maximum tangential velocity. Most of the variation is concentrated around $C_d = 0.035$, where the $v$ field adjusts from largely one-celled to mostly two-celled (Fig. 14). The simulations for $S_r = 0.01$ present the same structural transitions previously listed, starting from the vortex breakdown onward (Fig. 13). For vortex breakdown solutions with $S_r = 0.01$, the single-celled portion of the vortex weakens as the interface between the one-celled and two-celled regions descends; therefore, maxima are found at a larger radius from the core instead of directly below the vortex breakdown. This is in contrast with the intensification of the lowest region of the vortex observed for $S_r = 0.005$. This difference between the two cases will be examined in the following section. As a result of this behavior, the sharp
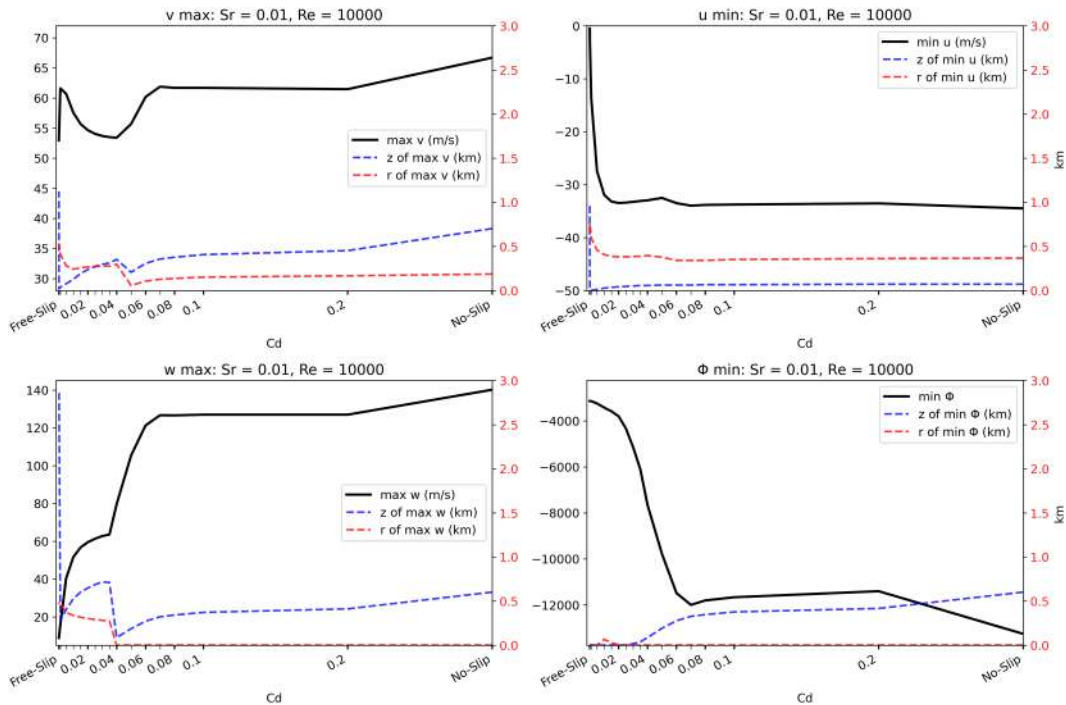
FIG. 13. As in Fig. 10, but for $S_r = 0.01$.

change from the tightening of the one-celled vortex to the enlargement of the two-celled vortex following the transition to a two-celled structure is masked by the sudden shift in the position of the extrema. Despite this behavior making it harder to see the transition in Fig. 13 compared to Fig. 10, the structure of the vortex is made clearer by looking at the fields. For instance, visualizing the tangential velocity for $C_d = 0.035$ (Fig. 14), it is evident that for this value of the drag coefficient,
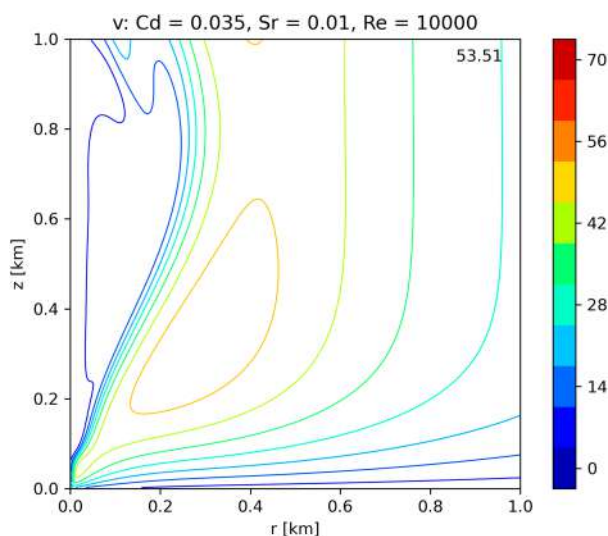


FIG. 14. Tangential velocity $v$ contour lines in the 1 km × 1 km window from the origin for $S_r = 0.01$, Re = 10 000, and $C_d = 0.035$.

the vortex undergoes breakdown, with the single-celled region reduced to the area below $z \approx 0.1$ km and the two-celled portion exhibiting larger values of tangential velocity. Combining the information from Figs. 13 and 14, we obtain once again that a reduction in $C_d$ causes the same structural changes observed for an increase of $S_r$ under no-slip conditions: starting from a single-celled structure, the vortex undergoes breakdown, and its position descends. As the vortex breakdown reaches the surface, the vortex exhibits a two-celled structure. Finally, a further decrease in $C_d$ leads to an enlargement of the vortex, and the solution tends to the free-slip case, with significantly reduced low-level updraft and inflow.

### 3) THE EFFECT OF $C_d$ ON THE STRUCTURE OF THE VORTEX FOR $S_r = 0.04$

Moving to the $S_r = 0.04$ simulations, we expect that a decrease in friction will continue to induce structural changes akin to those produced by a variation of swirl ratio for a fixed Re and under no-slip boundary conditions. For $S_r = 0.04$ and Re = 10 000, the no-slip solution is a two-celled vortex, as illustrated by the position of the yellow box in the parameter space of Fig. 7, firmly above the optimal vortex diagonal line. For very large swirl ratios, two-celled vortices lose their axial symmetry and break into satellite vortices revolving around the center axis (Rotunno 2013). Naturally, the present work's axisymmetric model is not capable of capturing this behavior. Therefore, it is reasonable to anticipate that the introduction of semislip conditions for $S_r = 0.04$ will not lead to any change in structure other than the previously described vortex
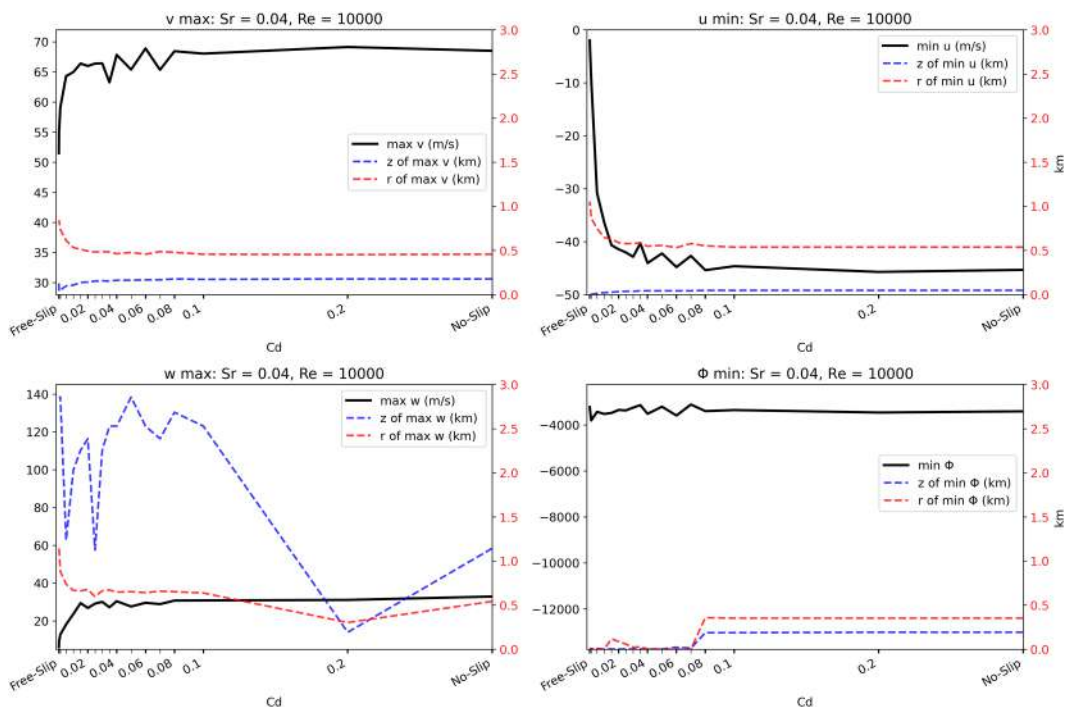
FIG. 15. As in Fig. 10, but for $S_r = 0.04$.

enlargement and convergence to the free-slip solution for $C_d \to 0$, but rather we expect the simulations to show more unsteadiness. Indeed, while remaining statistically stationary, the semislip simulations under lower friction showed increased unsteadiness.

Across the entire range of $C_d$ values explored, the vortex does not undergo structural modifications. The two-celled structure simulated under no-slip conditions is preserved for a decrease in friction. This behavior can be seen in Fig. 15, which displays the extremes of the fields. The tangential velocity field shows little variation in the magnitude of max($v$), before rapidly converging to the free-slip solution value. The increase in the radial position of max($v$) evidences a gradual enlargement of the vortex for decreasing $C_d$.

The radial and vertical velocities confirm these results, with min($u$) and max($w$) remaining stable across a wide range of $C_d$ values before steeply going to zero toward free-slip conditions. The radial position shows the same behavior as for the tangential velocity. The pressure field gives a clear indication of the preservation of a two-celled structure, as min($\phi$) remains very stable at a moderate value of pressure drop.

The progressive decrease in the vertical position of the extrema of the tangential and radial velocities is related to the increased shallowness of the boundary layer as $C_d$ decreases, which was described in section 4b. The large variation in the vertical position of max($w$) and the sudden jump in the location of min($\phi$) is a consequence of the increased homogeneity of these fields: different areas of the vortex have marginally different field magnitudes; hence, the extrema can be found at very different positions without an underlying change in the structure of the vortex.

### 4) FINAL REMARKS ON THE ROLE OF $C_d$ ON THE STRUCTURE OF THE VORTEX

The analysis of the semislip simulations reveals that the drag coefficient is a fundamental parameter in determining the structure of a vortex, suggesting that, under semislip conditions, the parameter space depicted in Fig. 7 is, in fact, three-dimensional, with $C_d$ being the third dimension. The results reveal that a decrease in $C_d$ for fixed $S_r$ and Re induces the same one-celled to two-celled transition that occurs for an increase in $S_r$ for fixed Re under no-slip conditions: a single-celled vortex undergoes vortex breakdown and transitions to a two-celled structure for increasing swirl ratio as well as for decreasing drag coefficient.

These results are confirmed by the study of the corner flow swirl ratio $S_c$. Unlike the swirl ratio used as a fundamental parameter, the corner flow swirl ratio focuses on the flow from the surface layer to the core, and it does not depend on the large-scale geometry (Lewellen et al. 2000; Lewellen and Lewellen 2007a,b). The vortex structure has been observed to be related to the value of $S_c$ relative to a critical value of $S_c$ (Lewellen et al. 2000), analytically found to be $S_c^* = 1.5$ (Bluestein 2013). For $S_c \ll S_c^*$, the structure is one-celled; for $S_c \gg S_c^*$, the vortex is two-celled; while for $S_c^*$, the vortex shows peak intensity (optimal vortex). By varying the roughness length $z_0$, Lewellen et al. (2000) found a decrease in $S_c$ when surface roughness is increased. Figure 16 shows the values of $S_c$ in the range of $C_d$ from 0.005 to 0.2 for $S_r = 0.005$ (circles) and $S_r = 0.01$ (crosses). The color of each point is determined by the ratio $\Phi/\Phi_{min}$, where $\Phi_{min}$ is the minimum pressure (i.e., the maximum magnitude of pressure drop) simulated across
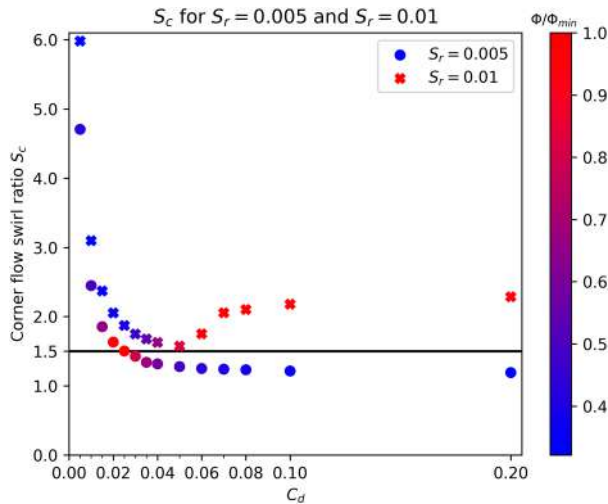
FIG. 16. Scatterplot of the corner flow swirl ratio $S_c$ as a function of $C_d$ for $S_r = 0.005$ (circles) and $S_r = 0.01$ (crosses). The color is related to the ratio $\Phi/\Phi_{min}$ of the pressure drop to the maximum pressure drop for a given $S_r$. The black solid line highlights the critical $S_c$, $S_c^* = 1.5$.

the whole $C_d$ range (including no-slip and free-slip cases) for a given value of $S_r$. The color goes from blue to red as the solutions approach the optimal vortex. We have highlighted $S_c^* = 1.5$ with a solid black line. Focusing on $S_c$ for $S_r = 0.005$, we can see that $S_c < S_c^*$ for high $C_d$ values, and it approaches the critical value for decreasing $C_d$, which is reached for $C_d = 0.025$. For this value of $C_d$, the vortex has maximum intensity, as evidenced by the high $\Phi/\Phi_{min}$ ratio. For $S_c > S_c^*$, a decrease in $C_d$ results in a reduced intensity, as the vortex structures evolve from breakdown events to two-celled vortices. Moving to the simulations for $S_r = 0.01$, we preliminarily note the large difference in $S_c$ for no-slip conditions ($S_c = 1.25$, not shown) and for the largest $C_d$ value explored in this study ($S_c = 2.29$ for $C_d = 0.2$). The no-slip case is well below the critical value, indicating a one-celled structure, while the $C_d = 0.2$ case is above $S_c^*$, and the vortex undergoes vortex breakdown. This is in agreement with the hypothesis of the optimal vortex occurring for larger $C_d$ values than those explored in this work. We notice that for $S_r = 0.01$, $S_c$ is always larger than $S_c^*$ and that the intensity decreases as $C_d$ is diminished. These results are in agreement with the previous analysis.

For a fixed Re, the structure of a vortex is defined by the position of its solution in the $S_r$–$C_d$ parameter space. A possible consequence of this result is that the optimal vortex line, described in Rotunno et al. (2016), might be a slanted surface in the three-dimensional parameter space. However, it is important to remark that in this work, we studied the consequences of semislip conditions for only three $S_r$–Re combinations. Therefore, further research is needed to assess the details of this three-dimensional parameter space.

### d. Analysis of the corner flow region

In the previous section, we highlighted how a decrease in friction for the $S_r = 0.005$ and $S_r = 0.01$ semislip simulations causes an intensification of all the fields in the vicinity of the

origin, as long as the solution has not reached a full two-celled structure. In particular, for $S_r = 0.005$, this intensification leads to a peak in the intensity of all fields, with magnitudes larger than the extrema of both the no-slip and free-slip cases. This region of the domain is usually referred to as the "corner flow region" and is characterized by both the radial and vertical pressure gradients being significantly different from zero. Unfortunately, the study of the corner flow is challenging due to the stationarity of the solution and the fact that almost every term of the Navier–Stokes equations is important. The region near the origin must reflect the properties of the radial inward flow that is located upstream; therefore, we can focus on the region of the inflow instead.

#### 1) DERIVATION OF A SIMPLIFIED SET OF EQUATIONS

To study the radial inflow, we will obtain a simplified set of equations. Since the horizontal diffusion for both the radial and tangential components of the Navier–Stokes equations is negligible for $r > 0.25$ km, we can work with simplified equations limiting ourselves to the region $r > 0.25$ km. Moreover, the inflow lies outside of the damping region of the domain; thus, the damping term can be neglected. Finally, once the simulation has reached a steady state, the Coriolis component becomes numerically negligible with respect to the other terms of the equations. With these assumptions, the radial component of the cylindrical Navier–Stokes equation [(3a)] is

$$\frac{du}{dt} = -\frac{\partial \phi}{\partial r} + \frac{v^2}{r} + \frac{1}{\rho}\frac{\partial \tau_{rz}}{\partial z}, \tag{9}$$

where $-\partial\phi/\partial r$ is the pressure gradient, $v^2/r$ is the centrifugal acceleration, and $\partial\tau_{rz}/\rho\partial z$ is the vertical diffusion. For simplicity, we will define $\partial\phi/\partial r = P$ and $v^2/r = C$:

$$\frac{du}{dt} = [-P + C] + \frac{1}{\rho}\frac{\partial \tau_{rz}}{\partial z}. \tag{10}$$

We note that, when $P > C$, the pressure gradient drives an inward radial flow, whereas for $P < C$, the centrifugal acceleration drives an outward radial flow. Now we take a vertical average, integrating between $z = 0$ and $z = \delta$, where $\delta$ is the height of the upper limit of the lower tier of the boundary layer. We have seen in section 4b that the upper limit of the lower layer (frictional layer) is the height of the maximum of $-ur$, therefore characterized by $\partial u/\partial z = 0$. The average yields as follows:

$$\overline{\frac{du}{dt}} = [-\overline{P} + \overline{C}] + \frac{1}{\delta\rho}\int_0^\delta \frac{\partial \tau_{rz}}{\partial z}\,dz, \tag{11}$$

where

$$\overline{(...)} = \frac{1}{\delta}\int_0^\delta (...)dz. \tag{12}$$

Solving the integral, we obtain

$$\frac{1}{\delta\rho}\int_0^\delta \frac{\partial \tau_{rz}}{\partial z}\,dz = \frac{1}{\delta\rho}(\tau_{rz}|_{z=\delta} - \tau_{rz}|_{z=0}). \tag{13}$$

Substituting the formulation for $\tau_{rz}$ at $z = \delta$, we notice that since $\partial u/\partial z = 0$ at $z = \delta$,

$$\tau_{rz}|_{z=\delta} = \nu\rho\left(\frac{\partial u}{\partial z}\bigg|_{z=\delta} + \frac{\partial w}{\partial r}\bigg|_{z=\delta}\right) = \nu\rho\frac{\partial w}{\partial r}\bigg|_{z=\delta} \approx 0. \quad (14)$$

The vertical average allows us to simplify the equation, limiting the vertical diffusion to its surface contribution. In the present work, the model computes $\tau_{rz}$ at $z = 0$ under semislip conditions as

$$\tau_{rz}|_{z=0} = \rho u_*^2 \frac{u}{V}\bigg|_{z=0}, \quad (15)$$

where $V$ is the surface velocity

$$V = \sqrt{u^2 + v^2}|_{z=0}, \quad (16)$$

and $u_*$ is the friction velocity, computed by the model as

$$u_* = \frac{\kappa V}{\ln\dfrac{2.5 + z_0}{z_0}}. \quad (17)$$

In Eq. (17), $\kappa = 0.40$ is the von Kármán constant; 2.5 is the height of the first grid point in meters, where this calculation is carried out; and $z_0$ is the roughness length (Lumley and Panofsky 1964, chapter 3.3)

$$z_0 = \frac{10}{\exp\left(\dfrac{\kappa}{\sqrt{C_d}}\right) - 1}, \quad (18)$$

where the number 10 appears because the estimate of $z_0$ is conventionally carried out at 10 m. Substituting, Eq. (11) becomes

$$\frac{\overline{du}}{dt} = [-\overline{P} + \overline{C}] - \frac{1}{\delta}u_*^2\frac{u}{\sqrt{u^2 + v^2}}\bigg|_{z=0}. \quad (19)$$

Equation (19) can be written in a more concise way by using the property $u_*^2 = C_d V^2$ (Lumley and Panofsky 1964, chapter 3.3)

$$\frac{\overline{du}}{dt} = [-\overline{P} + \overline{C}] - \frac{1}{\delta}(C_d V u)\bigg|_{z=0}. \quad (20)$$

It is worth highlighting the formulation of the vertical diffusion in Eq. (20), with $C_d$ multiplying $V$. A decrease in friction increases the surface velocity $V$ while decreasing $C_d$. Since the behaviors of $C_d$ and $V$ are in opposition, the outcome of a decrease in friction is nontrivial.

The tangential component of the cylindrical Navier–Stokes equation [(3b)] can be simplified using the same assumptions as for the $u$ equation:

$$\frac{dv}{dt} = -\frac{uv}{r} + \frac{1}{\rho}\frac{\partial\tau_{\theta z}}{\partial z}, \quad (21)$$

where $-uv/r$ is the centrifugal acceleration and $\partial\tau_{\theta z}/\rho\partial z$ is the vertical diffusion. Multiplying by $r$ and rearranging,

$$\frac{d(rv)}{dt} = \frac{d\Gamma}{dt} = \frac{1}{\rho}\frac{\partial(r\tau_{\theta z})}{\partial z}. \quad (22)$$

We can now take the vertical average, using the operator defined in Eq. (12) and employing the formulations of $\tau$ described for the $u$ equation in Eqs. (14) and (15). The result of the average is

$$\frac{\overline{d\Gamma}}{dt} = \frac{1}{\delta}\left(\nu\frac{\partial\Gamma}{\partial z}\bigg|_{z=\delta} - u_*^2\frac{\Gamma}{\sqrt{u^2 + v^2}}\bigg|_{z=0}\right), \quad (23)$$

which can be written in a more concise way as follows:

$$\frac{\overline{d\Gamma}}{dt} = \frac{1}{\delta}\left(\nu\frac{\partial\Gamma}{\partial z}\bigg|_{z=\delta} - (C_d V\Gamma)\bigg|_{z=0}\right). \quad (24)$$

Combining Eqs. (19) and (23), we obtain the set of equations employed in this section:

$$\begin{cases} \dfrac{\overline{du}}{dt} = [-\overline{P} + \overline{C}] - \dfrac{1}{\delta}u_*^2\dfrac{u}{\sqrt{u^2 + v^2}}\bigg|_{z=0} \\[3mm] \dfrac{\overline{d\Gamma}}{dt} = \dfrac{1}{\delta}\left(\nu\dfrac{\partial\Gamma}{\partial z}\bigg|_{z=\delta} - u_*^2\dfrac{\Gamma}{\sqrt{u^2 + v^2}}\bigg|_{z=0}\right) \end{cases}. \quad (25)$$

It must be remarked that the use of the $\partial u/\partial z = 0$ property of the frictional layer's upper limit does not imply that the equations are valid only in the region where the potential vortex assumption holds. The requirement for this set of equations to be valid is simply the existence of the two-tiered structure of the boundary layer. Indeed, the two-tiered structure exists even for $r < 1$ km. Figure 17 shows an example for $S_r = 0.005$ and $C_d = 0.2$. The boundary layer does not exhibit the radial behavior of a potential vortex boundary layer, as the lower tier has almost the same thickness for $z = 0.25$, $z = 0.5$, and $z = 1$ km, in agreement with the results of section 4a, where the potential vortex region was always found to extend from $r \gtrsim 1$ km. This property of $\delta \approx$ const is useful, allowing one to employ a fixed upper limit of integration $\delta$. The black horizontal line in Fig. 17 represents the height of the upper limit of the lower tier for $r = 0.25$ km, which is the same for $r = 0.5$ km, while the height for $r = 1$ km differs by only one grid spacing. More generally, for any fixed $C_d$ value between 0.2 and 0.035, $\delta$ does not vary by more than two grid points through the $0.25 < r < 1$ km range for $S_r = 0.005$ and $S_r = 0.01$. This property is degraded for $C_d < 0.035$; therefore, we limit the analysis to the $0.035 \leq C_d \leq 0.2$ range. We note that, for these values of $C_d$, the $S_r = 0.005$ simulations represent a single-celled vortex, whereas for $S_r = 0.01$, the vortex undergoes breakdown. We further limit the domain of the analysis to $0.25 < r < 0.95$ km to avoid the numerical noise introduced by the change in grid spacing that occurs at $r = 1$ km.
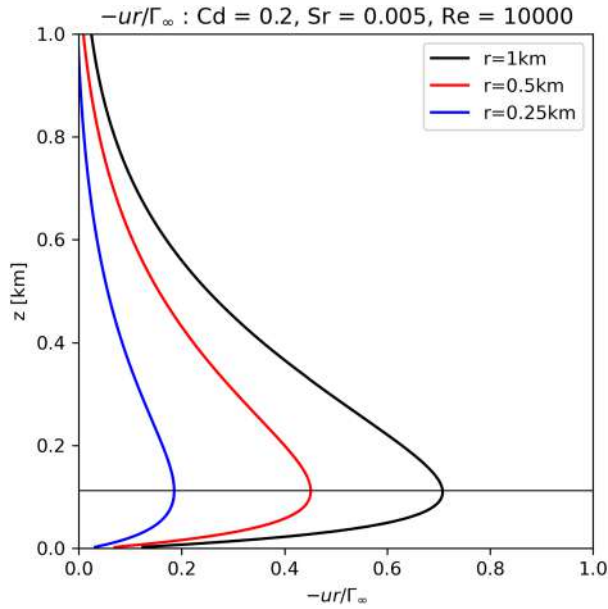
FIG. 17. Vertical profiles of $-ur/\Gamma_\infty$ for $S_r = 0.005$, $Re = 10\,000$, and $C_d = 0.2$ sampled at 1 km (black), 0.5 km (red), and 0.25 km (blue). The horizontal black line illustrates the upper limit of the lower tier for the profiles sampled at 0.5 and 0.25 km.

For simplicity, we will introduce the following notations as follows:

$$\begin{cases} \text{term}_1 = [-\overline{P} + \overline{C}] \\ \text{term}_2 = -\dfrac{1}{\delta} u_*^2 \dfrac{u}{\sqrt{u^2 + v^2}}\Big|_{z=0} \\ \text{term-}z_1 = \dfrac{\nu}{\delta}\dfrac{\partial \Gamma}{\partial z}\Big|_{z=\delta} \\ \text{term-}z_0 = -\dfrac{u_*^2}{\delta}\dfrac{\Gamma}{\sqrt{u^2 + v^2}}\Big|_{z=0} \end{cases} . \tag{26}$$

In the first of Eq. (25), $\text{term}_1$ represents the sum of the radial pressure gradient and the centrifugal acceleration, while $\text{term}_2$ is the contribution of the surface drag. The sum of $\text{term}_1$ and $\text{term}_2$ represents the vertical average of the total derivative of $u$. In the second of Eq. (25), term $z_1$ is related to the vertical gradient of $\Gamma$ at $z = \delta$, while term $z_0$ is the contribution of the surface drag to the $\Gamma$ equation. The sum of term $z_1$ and term $z_0$ represents the vertical average of the total derivative of $\Gamma$. In the $u$ equation,

$$\frac{\overline{du}}{dt} = \overline{\left( u\frac{\partial u}{\partial r} + w\frac{\partial u}{\partial z} \right)}, \tag{27}$$

and we empirically find that

$$\left| u\frac{\partial u}{\partial r} \right| \gg \left| w\frac{\partial u}{\partial z} \right| \tag{28}$$

in the region of interest. Therefore,

$$\frac{\overline{du}}{dt} = \overline{\left( u\frac{\partial u}{\partial r} \right)}. \tag{29}$$

Since $u < 0$ for the inflow, a negative value of the sum between $\text{term}_1$ and $\text{term}_2$ indicates an intensification of the inflow moving inward. The radius for which the sum is zero represents the radial position of the inflow's strongest region. Moving inward from $r = 0.95$ km, we expect a negative value of the average of $du/dt$, which eventually goes to zero, before attaining positive values in the stagnation area, where the inflow is stopped and turned. We anticipate $\text{term}_1$ to be negative where the pressure gradient drives the radial inflow and positive in the stagnation area, where the flow is gradually stopped. The surface friction $\text{term}_2$ is expected to always be positive, as it opposes the inward flow. In the $\Gamma$ equation,

$$\frac{\overline{d\Gamma}}{dt} = \overline{\left( u\frac{\partial \Gamma}{\partial r} + w\frac{\partial \Gamma}{\partial z} \right)}, \tag{30}$$

and, similarly to Eq. (28), we empirically find that, in the region of interest,

$$\left| u\frac{\partial \Gamma}{\partial r} \right| \gg \left| w\frac{\partial \Gamma}{\partial z} \right|. \tag{31}$$

Thus,

$$\frac{\overline{d\Gamma}}{dt} = \overline{\left( u\frac{\partial \Gamma}{\partial r} \right)}, \tag{32}$$

and since $u < 0$ and $\Gamma$ decreases moving inward, we expect the sum between term $z_1$ and term $z_0$ to be always negative. The angular momentum increases with height; thus, we anticipate term $z_1$ to be always positive. Finally, term $z_0$ is the dissipation of angular momentum, a negative quantity.

2) ANALYSIS OF THE CORNER FLOW REGION FOR $S_r = 0.005$

Figure 18 presents the terms of Eq. (25) for $S_r = 0.005$. In the left column, the $u$ equation is described by plotting $\text{term}_1$ in blue, $\text{term}_2$ in orange, and the sum of the two terms in magenta. In the right column, the $\Gamma$ equation is depicted with term $z_1$ in blue, term $z_0$ in orange, and the sum of the terms in magenta. The top row is for $C_d = 0.2$, and the bottom row is for $C_d = 0.035$. Studying the left column, we note how the radius where the sum intersects with zero, representing the position of maximum inflow intensity, shifts to smaller radii as drag is reduced. The shift reveals how the decrease in drag enables the inflow to reach deeper into the corner flow region, closer to the origin. A similar shift is observed for the minimum of the average of $du/dt$, indicating that the maximum inflow strengthening occurs closer to the origin. A significant increase in the magnitude of the minimum is also found, with the average of $du/dt$ increasing from $-0.072$ m s$^{-2}$ for $C_d = 0.2$ to $-0.169$ m s$^{-2}$ for $C_d = 0.035$. These results suggest that a decrease in drag causes the inflow to intensify and move closer to the origin. Notably, $\text{term}_2$ decreases toward
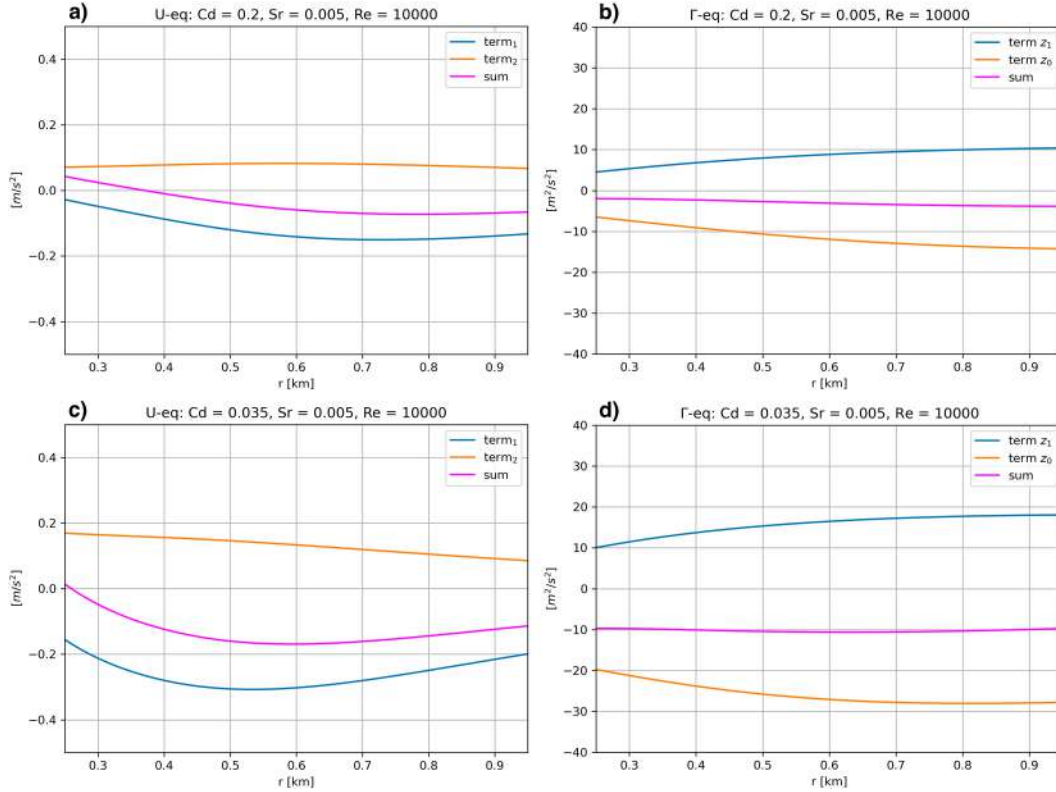
FIG. 18. Radial profiles from $r = 0.25$ km to $r = 0.95$ km of the terms of Eq. (25) [as defined in Eq. (26)] for $S_r = 0.005$ and Re $= 10\,000$: (a),(c) term$_1$ (blue), term$_2$ (orange), and their sum (magenta) (m s$^{-2}$); (b),(d) term $z_1$ (blue), term $z_0$ (orange), and their sum (magenta) (m$^2$ s$^{-2}$). (a),(b) $C_d = 0.2$; (c),(d) $C_d = 0.035$.

the origin for $C_d = 0.2$, whereas it increases for $C_d = 0.035$. Since term$_2$ depends only on $C_d$ and surface velocity [Eq. (20)], for constant $C_d$, the variation is due to the behavior of the surface velocity, indicating that for decreasing drag, the surface velocity near the origin increases. This confirms the results of section 4b, where the increased magnitude of all the fields in proximity to the origin for decreasing $C_d$ was highlighted.

The negative value of the average of $d\Gamma/dt$ (magenta line) indicates dissipation of angular momentum as parcels are advected toward the origin by the inflow. The second column of Fig. 18 shows that the dissipation of angular momentum becomes more intense as drag diminishes. At $r = 0.25$ km, the average of $d\Gamma/dt$ goes from $-1.964$ m$^2$ s$^{-2}$ for $C_d = 0.2$ to $-9.692$ m$^2$ s$^{-2}$ for $C_d = 0.035$. The fact that the dissipation becomes larger as $C_d$ diminishes suggests that the inflow brings parcels with larger $\Gamma$ toward the origin. From Eqs. (24) and (26), it can be seen that term $z_0$ depends on $\Gamma$; a larger magnitude reflects a larger value of $\Gamma$. This can be appreciated in Fig. 19, showing the $\Gamma$ field for $S_r = 0.005$ under no-slip conditions (left) and semislip conditions with $C_d = 0.035$ (right): The value of $\Gamma$ in the window of size 0.2 km starting from the origin becomes significantly larger for a lower drag coefficient. It is worth highlighting that while for $C_d = 0.2$, the magnitude of the average of $d\Gamma/dt$ decreases slightly as $r \to 0$, for $C_d = 0.035$, it remains steady. The decrease for $C_d = 0.2$ indicates that at $r = 0.25$ km, the parcel's angular momentum approaches zero,

and therefore, the rate of decrease weakens, whereas for $C_d = 0.035$, the angular momentum at $r = 0.25$ km is still significant, and the rate of decrease is steady.

The analysis of the $\Gamma$ equation gives us insights into the significant magnitude increase of term$_1$ for a decrease in $C_d$ in the $u$ equation (left column of Fig. 18). The advection of high $\Gamma$ parcels toward the corner flow region implies an increase in the centrifugal force, since $C = v^2/r = \Gamma^2/r^3$. The $\overline{C}$ gives a positive contribution to term$_1$; hence, the pressure gradient force has to dramatically increase in magnitude to produce more negative values of term$_1$. This explains the drastic intensification of the pressure drop depicted in Figs. 8 and 10.

The presence of a peak in the intensity of the maximum inflow as a function of $C_d$, noted in Fig. 10 for the simulations with $S_r = 0.005$, suggests the presence of two competing processes, one weakening the inflow for decreasing $C_d$ (leading to the convergence of the solution to the free-slip case for $C_d \to 0$) and the other strengthening it (causing the rapid inflow intensification leading to the peak). This results in two regimes, one for $C_d > C_{d\text{peak}}$, where the weakening process dominates, and the other for $C_d > C_{d\text{peak}}$, where the strengthening process dominates. The competing effects seen in the two regimes are evident rewriting term$_2$ using the formulation of Eq. (20) as follows:
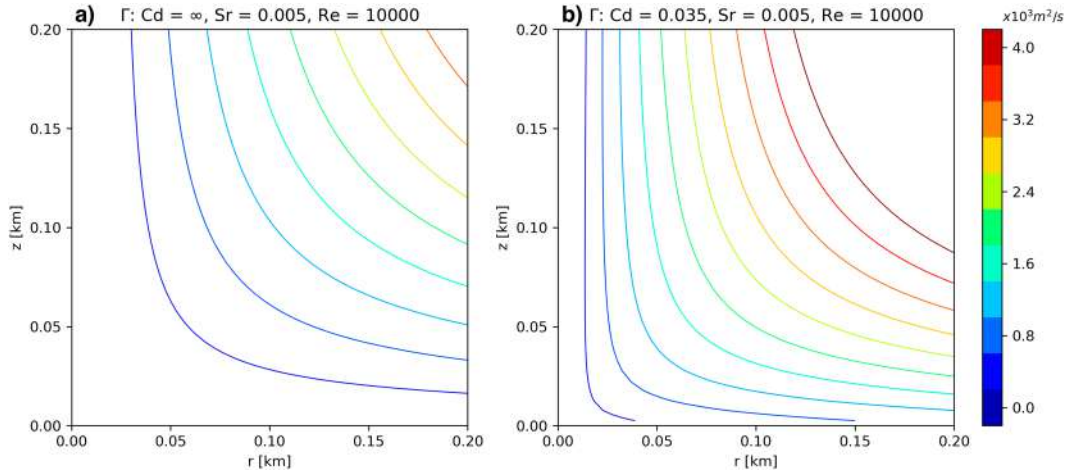
$$-C_d \times V \times u|_{z=0}. \tag{33}$$

FIG. 19. Angular momentum $\Gamma$ (m$^2$ s$^{-1}$) contour lines in the 0.2 km $\times$ 0.2 km window from the origin for $S_r = 0.005$, Re = 10 000 under (a) no-slip ($C_d = \infty$) conditions and (b) semislip conditions with $C_d = 0.035$.

For $C_d > C_{d\text{peak}}$, the weakening of peak intensity is the result of the crucial role played by vertical diffusion in balancing the pressure gradient at the surface, leading to the presence of an inflow (Rotunno 2013) (in the absence of surface stress, the inward pressure gradient is exactly balanced by the centrifugal force). Clearly, a reduction in $C_d$ in this regime leads to a weakening of the inflow. For $C_d > C_{d\text{peak}}$, the simulations for $S_r = 0.005$ suggest that a decrease in $C_d$ allows the surface velocity $V$ to increase substantially (Fig. 9). In this case, the drag increases (term$_2$ in Fig. 18) but allows the aforementioned imbalance between the pressure gradient and centrifugal force (term$_1$) to produce a stronger inflow. Along with the intensification of the inflow, a reduction in drag implies a smaller depletion of the angular momentum of the inflow, and parcels with larger $\Gamma$ are advected toward the origin. Since $\Gamma = rv$, the advection of parcels with large $\Gamma$ enhances the swirling motion near the origin, contributing to the larger $V$ in Eq. (33). The $C_d > C_{d\text{peak}}$ regime is effectively a feedback between the boundary layer and the pressure gradient in the corner flow region. The resulting enhanced inflow is driven closer to the origin and forced to perform a tighter turn, as evidenced by the streamlines in Fig. 8, producing a funneling effect that contributes to the intensification of the updraft, explaining the significant intensification as $C_d > C_{d\text{peak}}$ seen in Figs. 9 and 10.

The results presented in Fig. 18 show that in the regime for $C_d > C_{d\text{peak}}$, a decrease in $C_d$ results in a strengthening of the inflow, which due to the reduced drag brings parcels with larger angular momentum near the origin. The competing processes occurring for decreasing $C_d$ give rise to a peak in intensity of all fields, explaining the peaking behavior of the extrema shown in Fig. 10. We note that this behavior is compatible with an increase in the corner flow swirl ratio $S_c$ for decreasing $C_d$ for a subcritical vortex, and $C_{d\text{peak}}$ represents the $C_d$ value resulting in an optimal vortex (Fig. 16).

3) ANALYSIS OF THE CORNER FLOW REGION FOR $S_r = 0.01$

In section 4c, the extrema of the fields for $S_r = 0.01$ (Fig. 13) did not exhibit the same peaking behavior as for $S_r = 0.005$. Instead, the maximum tangential velocity and the minimum radial velocity showed marginal weakening of the swirling motion and the inflow. It is therefore interesting to perform the same analysis on the $S_r = 0.01$ simulations.

In stark contrast to the $S_r = 0.005$ case, the left column of Fig. 20 shows marginal changes in the radial profile of the average of $du/dt$ for decreasing $C_d$. The point where the sum intersects with zero does not shift toward the origin for decreasing friction but instead moves to a slightly larger radius. The magnitude of the minimum of the average of $du/dt$ shows minimal variation, going from $-0.598$ m s$^{-2}$ for $C_d = 0.2$ to $-0.575$ m s$^{-2}$ for $C_d = 0.035$. The results show that for $S_r = 0.01$, the competing effects do not cause an intensification of the inflow, which instead remains mostly unchanged. On the other hand, the right column illustrates that a decrease in drag causes an increase in the magnitude of the average of $d\Gamma/dt$, similarly to the $S_r = 0.005$ case. Quantitatively, the average of $d\Gamma/dt$ at $r = 0.25$ km diminishes from $-8.095$ m$^2$ s$^{-2}$ at $C_d = 0.2$ to $-20.213$ m$^2$ s$^{-2}$ at $C_d = 0.035$. The fact that for both $S_r = 0.005$ and $S_r = 0.01$, a decrease in surface drag leads to parcels attaining larger values of angular momentum near the origin explains the observed increase in tangential velocity in the vicinity of the origin.

The present analysis confirms the differences between the $S_r = 0.005$ and $S_r = 0.01$ semislip simulations observed in section 4c. While for $S_r = 0.005$, the inflow intensifies and shifts toward the origin for decreasing drag within the range $C_d = 0.2$–0.035, for $S_r = 0.01$, the inflow remains mostly unchanged. The occurrence of the inflow strengthening and shift appears to be related to the value of the swirl ratio, and in particular to the vortex structure, which is related to the $S_r$ value (Rotunno et al. 2016). In fact, we have emphasized the different structures of the two cases: While for $S_r = 0.005$, the
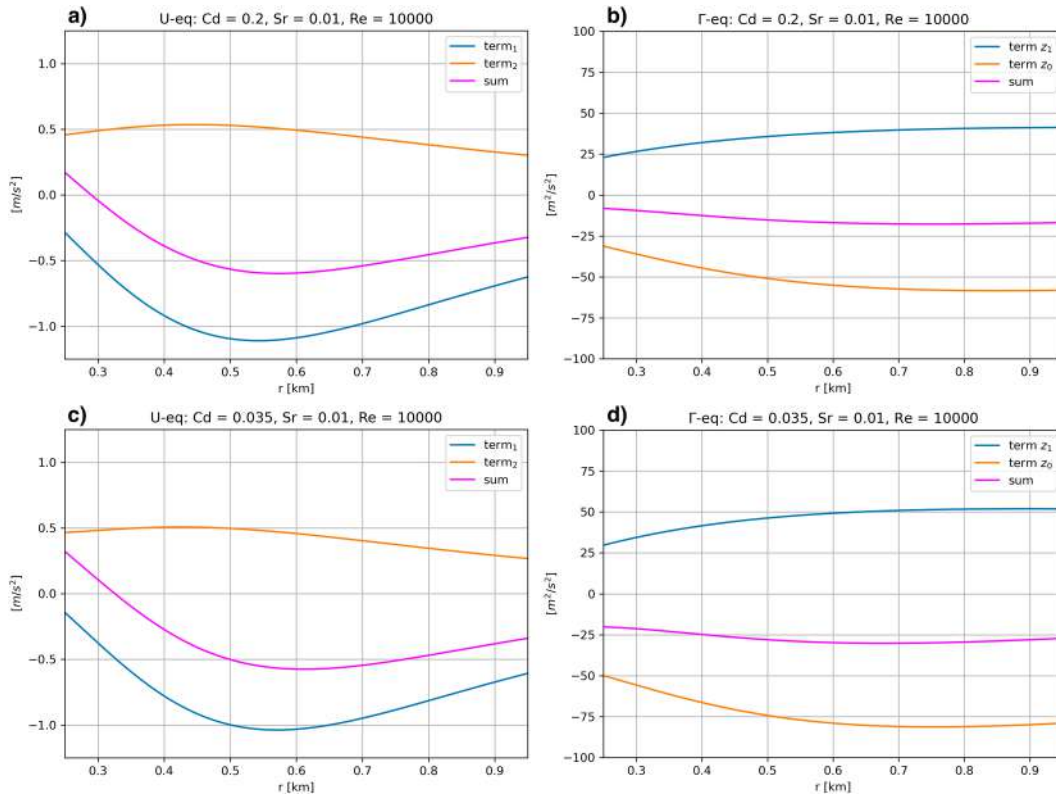
FIG. 20. As in Fig. 18, but for $S_r = 0.01$.

vortex is single-celled up to $C_d = 0.03$, for $S_r = 0.01$, the vortex undergoes breakdown throughout the $C_d$ range examined. This also means that in this $C_d$ range, the $S_r = 0.005$ vortices are subcritical, while the ones for $S_r = 0.01$ are supercritical (Fig. 16). As mentioned in section 4c, since the vortex breakdown for $S_r = 0.01$ is observed for the highest $C_d$ value employed in this study, it is unclear if the inflow strengthening happens for higher friction. To better understand this phenomenon, more simulations are needed. In particular, the present results suggest that investigating the range $S_r = 0.005$–0.01 can provide important information on the matter.

## 5. Conclusions

In the present work, we investigated the effect of semislip lower boundary conditions on simulated supercell tornadoes, employing the same axisymmetric approach used in Rotunno et al. (2016) and using 16 values of drag coefficient from $C_d = 0.02$ to $C_d = 0.0001$ to bridge the gap between no-slip and free-slip conditions. The simulations for each $C_d$ value, as well as the no-slip and free-slip cases, have been carried out using a constant value of Re = 10 000 and three values of the swirl ratio, namely, $S_r = 0.005$, 0.01, and 0.04. The simulations have highlighted the following results:

- The potential vortex structure is preserved under semislip conditions: The angular momentum per unit mass is approximately constant in the region $1 \lesssim r \lesssim 2$ km and $1 \lesssim z \lesssim 2$ km.

- The lower tier of the potential vortex boundary layer becomes thinner for decreasing $C_d$, vanishing between $C_d = 0.005$ and $C_d = 0.001$.

- A decrease in $C_d$ for fixed $S_r$ and Re leads to the same structural transitions previously observed for increasing $S_r$ and fixed Re under no-slip conditions (Rotunno et al. 2016; Ward 1972): For the combinations of $S_r$–Re yielding one-celled vortices under no-slip conditions (Re = 10 000, $S_r = 0.005$, 0.01), a reduction in surface drag leads to the occurrence of a vortex breakdown, followed by a transition to a two-celled structure. For $S_r = 0.04$, the no-slip case is a two-celled vortex, and a decrease in friction does not lead to any further transition, in complete analogy to an increase in $S_r$ for two-celled vortices under no-slip conditions. These results are qualitatively in agreement with those of Fiedler (2017) and indicate that the drag coefficient plays a fundamental role in determining the structure of the vortex. They suggest that the $S_r$–Re parameter space used in previous no-slip studies should be expanded to the $S_r$–Re–$C_d$ space with the inclusion of the drag coefficient. The vortex structure would be determined by the values of the parameters in the 3D space. Figure 21 summarizes schematically the dependence of the vortex structure on $S_r$ and $C_d$ for constant Re.

- For the range of experiments explored here, the adoption of semislip boundary conditions results in a more accurate representation of the lowest levels of a tornado. In particular, for $S_r = 0.005$ and realistic values of $C_d$, the maximum
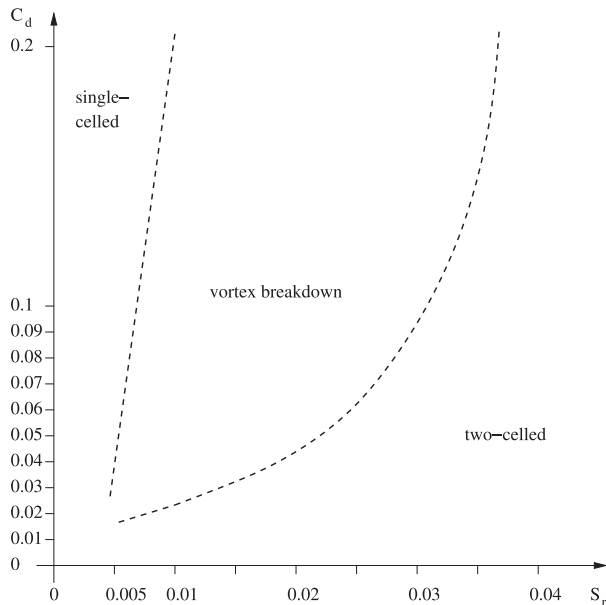
FIG. 21. Schematic diagram of the vortex structures in the $S_r$–$C_d$ parameter space. A decrease in $C_d$ (from top to bottom) results in the same transitions as an increase in $S_r$ (from left to right).

tangential wind speed can be found at very low levels, with a minimum of 12.5 m above the ground. Since the grid spacing close to the ground is 5 m, this represents just the third vertical grid point. This is a significant improvement over no-slip conditions, which lead to weaker winds near the surface compared to upper levels. The simplicity of no-slip conditions has previously been instrumental in developing the basic fluid dynamic theory of tornadoes using idealized axisymmetric vortex simulations. In this study, we improved the understanding of the lowest levels of tornadoes by employing semislip conditions. The accurate representation of the lowest levels of a tornado is crucial since the near-surface winds are the cause of the damage and loss of lives brought by these extreme weather phenomena. Recent Doppler on Wheels measurements (Kosiba and Wurman 2023) are in qualitative agreement with the present results for $S_r = 0.005$ and reasonable $C_d$ values, indicating that the strongest tornado winds are measured at the lowest levels (<15 m above ground level).

- For subcritical vortices, a decrease in the drag coefficient leads to an intensification of the vortex. A reduction in drag strengthens and shifts the inflow toward the center of the vortex, while the reduced dissipation of angular momentum allows the advection by the inflow of parcels with large angular momentum toward the vicinity of the origin. The combination of these two effects results in a significant intensification of the swirling motion, while the proximity of the inflow to the center of the vortex forces the inward flow to be funneled tightly into the updraft, boosting the intensity of the vertical velocity. Rotunno (1979) and, subsequently, Lewellen et al. (2000) described this corner flow behavior for subcritical vortices approaching the critical corner

flow swirl ratio $S_c^*$ and mentioned that surface drag would play a role by participating in the depletion of angular momentum; the present study highlighted how the vortex intensification for decreasing $C_d$ stems from the positive feedback between the boundary layer and the corner region pressure gradient. This effect has been observed for $S_r = 0.005$ (subcritical vortex) but not for $S_r = 0.01$ (supercritical vortex), suggesting that the vortex structure and the value of the corner flow swirl ratio $S_c$ relative to $S_c^*$ might play a role.

- The subcritical tornadoes under semislip conditions are more intense than the limiting cases of no-slip and free-slip conditions.

The limitation of the method followed in this work is that the experimental setup employs somewhat artificial assumptions, with a steady-state, axisymmetric approach, a prescribed forcing in lieu of the buoyancy acceleration, and a linear damping near the impermeable top boundary instead of the tropopause. Although artificial, these assumptions allow us to simplify the complex dynamics of a tornado-producing supercell, enabling us to investigate the dynamics of tornadoes at a reasonable computational cost. Notably, the assumptions lead to potential vortex radial profiles of tangential winds, in agreement with the profiles observed for natural tornadoes (Tanamachi et al. 2007). Liu and Ishihara (2016) studied the role of roughness on tornado-like vortices using a more realistic large-eddy simulation (LES) approach. Their comparison of the time-averaged flow with smooth and rough surfaces (their Figs. 12, 14, 15, and 17) is qualitatively consistent with the present results. This supports our use of a simplified and idealized approach, which allowed the physical interpretations in section 4d.

Additional simulations could offer greater insights into the role of the surface drag on tornadoes. It would be particularly valuable to explore the full three-dimensional parameter space, varying Re also. Moreover, further simulations in the range of swirl ratios from one-celled to vortex breakdown are needed to better understand the role of vortex structure in the intensification for decreasing $C_d$.

The use of semislip lower boundary conditions in the study of supercell tornadoes has increased considerably in recent years, replacing the no-slip and free-slip conditions previously employed. We believe that the results obtained in the present work could prove useful, providing information on the role of semislip conditions in simulated tornadoes.

measurements and modeling for strong WIND nowcast and RISK mitigation (WIND RISK)."

*Data availability statement.* The data used in this paper are available from the author upon request.

## REFERENCES

Alexander, C. R., and J. M. Wurman, 2008: Updated mobile radar climatology of supercell tornado structures and dynamics. *24th Conf. on Severe Local Storms*, Desoto, TX, Amer. Meteor. Soc., 19.4, https://ams.confex.com/ams/24SLS/webprogram/Paper141821.html.

Ashley, W. S., and S. M. Strader, 2016: Recipe for disaster: How the dynamic ingredients of risk and exposure are changing the tornado disaster landscape. *Bull. Amer. Meteor. Soc.*, **97**, 767–786, https://doi.org/10.1175/BAMS-D-15-00150.1.

Batchelor, G. K., 2000: *An Introduction to Fluid Dynamics*. Cambridge University Press, 615 pp., https://doi.org/10.1017/CBO9780511800955.

Bluestein, H. B., 2013: *Severe Convective Storms and Tornadoes: Observations and Dynamics*. Springer, 456 pp.

Borges, R., M. Carmona, B. Costa, and W. S. Don, 2008: An improved weighted essentially non-oscillatory scheme for hyperbolic conservation laws. *J. Comput. Phys.*, **227**, 3191–3211, https://doi.org/10.1016/j.jcp.2007.11.038.

Bryan, G. H., and J. M. Fritsch, 2002: A benchmark simulation for moist nonhydrostatic numerical models. *Mon. Wea. Rev.*, **130**, 2917–2928, https://doi.org/10.1175/1520-0493(2002)130%3C2917:ABSFMN%3E2.0.CO;2.

——, N. A. Dahl, D. S. Nolan, and R. Rotunno, 2017: An eddy injection method for large-eddy simulations of tornado-like vortices. *Mon. Wea. Rev.*, **145**, 1937–1961, https://doi.org/10.1175/MWR-D-16-0339.1.

Burggraf, O. R., K. Stewartson, and R. Belcher, 1971: Boundary layer induced by a potential vortex. *Phys. Fluids*, **14**, 1821–1833, https://doi.org/10.1063/1.1693691.

Church, C. R., J. T. Snow, G. L. Baker, and E. M. Agee, 1979: Characteristics of tornado-like vortices as a function of swirl ratio: A laboratory investigation. *J. Atmos. Sci.*, **36**, 1755–1776, https://doi.org/10.1175/1520-0469(1979)036<1755:COTLVA>2.0.CO;2.

Fiedler, B. H., 1994: The thermodynamic speed limit and its violation in axisymmetric numerical simulations of tornado-like vortices. *Atmos.-Ocean*, **32**, 335–359, https://doi.org/10.1080/07055900.1994.9649501.

——, 1995: On modelling tornadoes in isolation from the parent storm. *Atmos.–Ocean*, **33**, 501–512, https://doi.org/10.1080/07055900.1995.9649542.

——, 2009: Suction vortices and spiral breakdown in numerical simulations of tornado-like vortices. *Atmos. Sci. Lett.*, **10**, 109–114, https://doi.org/10.1002/asl.217.

——, 2017: Axisymmetric tornado simulations with a semi-slip boundary. *Fluids*, **2**, 68, https://doi.org/10.3390/fluids2040068.

——, and R. Rotunno, 1986: A theory for the maximum windspeeds in tornado-like vortices. *J. Atmos. Sci.*, **43**, 2328–2340, https://doi.org/10.1175/1520-0469(1986)043%3C2328:ATOTMW%3E2.0.CO;2.

Gairola, A., G. T. Bitsuamlak, and H. M. Hangan, 2023: An investigation of the effect of surface roughness on the mean flow properties of "tornado-like" vortices using large eddy simulations. *J. Wind Eng. Ind. Aerodyn.*, **234**, 105348, https://doi.org/10.1016/j.jweia.2023.105348.

Klemp, J. B., and R. B. Wilhelmson, 1978: The simulation of three-dimensional convective storm dynamics. *J. Atmos. Sci.*, **35**, 1070–1096, https://doi.org/10.1175/1520-0469(1978)035%3C1070:TSOTDC%3E2.0.CO;2.

Kosiba, K. A., and J. Wurman, 2013: The three-dimensional structure and evolution of a tornado boundary layer. *Wea. Forecasting*, **28**, 1552–1561, https://doi.org/10.1175/WAF-D-13-00070.1.

——, and ——, 2023: The strongest winds in tornadoes are very near the ground. *Commun. Earth Environ.*, **4**, 50, https://doi.org/10.1038/s43247-023-00716-6.

Lewellen, D. C., and W. S. Lewellen, 2007a: Near-surface intensification of tornado vortices. *J. Atmos. Sci.*, **64**, 2176–2194, https://doi.org/10.1175/JAS3965.1.

——, and ——, 2007b: Near-surface vortex intensification through corner flow collapse. *J. Atmos. Sci.*, **64**, 2195–2209, https://doi.org/10.1175/JAS3966.1.

——, ——, and J. Xia, 2000: The influence of a local swirl ratio on tornado intensification near the surface. *J. Atmos. Sci.*, **57**, 527–544, https://doi.org/10.1175/1520-0469(2000)057<0527:TIOALS>2.0.CO;2.

Liu, Z., and T. Ishihara, 2016: Study of the effects of translation and roughness on tornado-like vortices by large-eddy simulations. *J. Wind Eng. Ind. Aerodyn.*, **151**, 1–24, https://doi.org/10.1016/j.jweia.2016.01.006.

Lumley, J. L., and H. A. Panofsky, 1964: *The Structure of Atmospheric Turbulence*. Interscience Publishers, 239 pp.

Natarajan, D., and H. Hangan, 2012: Large eddy simulations of translation and surface roughness effects on tornado-like vortices. *J. Wind Eng. Ind. Aerodyn.*, **104–106**, 577–584, https://doi.org/10.1016/j.jweia.2012.05.004.

Neakrase, L. D. V., and R. Greeley, 2010: Dust devils in the laboratory: Effect of surface roughness on vortex dynamics. *J. Geophys. Res.*, **115**, E05003, https://doi.org/10.1029/2009JE003465.

Nolan, D. S., 2005: A new scaling for tornado-like vortices. *J. Atmos. Sci.*, **62**, 2639–2645, https://doi.org/10.1175/JAS3461.1.

——, N. A. Dahl, G. H. Bryan, and R. Rotunno, 2017: Tornado vortex structure, intensity, and surface wind gusts in large-eddy simulations with fully developed turbulence. *J. Atmos. Sci.*, **74**, 1573–1597, https://doi.org/10.1175/JAS-D-16-0258.1.

Orf, L., 2019: A violently tornadic supercell thunderstorm simulation spanning a quarter-trillion grid volumes: Computational challenges, I/O framework, and visualizations of tornadogenesis. *Atmosphere*, **10**, 578, https://doi.org/10.3390/atmos10100578.

——, R. Wilhelmson, B. Lee, C. Finley, and A. Houston, 2017: Evolution of a long-track violent tornado within a simulated supercell. *Bull. Amer. Meteor. Soc.*, **98**, 45–68, https://doi.org/10.1175/BAMS-D-15-00073.1.

Rotunno, R., 1979: A study in tornado-like vortex dynamics. *J. Atmos. Sci.*, **36**, 140–155, https://doi.org/10.1175/1520-0469(1979)036<0140:ASITLV>2.0.CO;2.

——, 2013: The fluid dynamics of tornadoes. *Annu. Rev. Fluid Mech.*, **45**, 59–84, https://doi.org/10.1146/annurev-fluid-011212-140639.

——, G. H. Bryan, D. S. Nolan, and N. A. Dahl, 2016: Axisymmetric tornado simulations at high Reynolds number. *J. Atmos. Sci.*, **73**, 3843–3854, https://doi.org/10.1175/JAS-D-16-0038.1.

Skamarock, W. C., and J. B. Klemp, 1992: The stability of time-split numerical methods for the hydrostatic and the nonhydrostatic elastic equations. *Mon. Wea. Rev.*, **120**, 2109–2127, https://doi.org/10.1175/1520-0493(1992)120<2109:TSOTSN>2.0.CO;2.

Smith, A. B., and J. L. Matthews, 2015: Quantifying uncertainty and variable sensitivity within the US billion-dollar weather and climate disaster cost estimates. *Nat. Hazards*, **77**, 1829–1851, https://doi.org/10.1007/s11069-015-1678-x.

Tanamachi, R. L., H. B. Bluestein, W.-C. Lee, M. Bell, and A. Pazmany, 2007: Ground-based velocity track display (GBVTD) analysis of W-band Doppler radar data in a tornado near Stockton, Kansas, on 15 May 1999. *Mon. Wea. Rev.*, **135**, 783–800, https://doi.org/10.1175/MWR3325.1.

Wang, A., Y. Pan, and P. M. Markowski, 2020: The influence of turbulence memory on idealized tornado simulations. *Mon. Wea. Rev.*, **148**, 4875–4892, https://doi.org/10.1175/MWR-D-20-0031.1.

——, ——, G. H. Bryan, and P. M. Markowski, 2023: Modeling near-surface turbulence in large-eddy simulations of a tornado: An application of thin boundary layer equations. *Mon. Wea. Rev.*, **151**, 1587–1607, https://doi.org/10.1175/MWR-D-22-0060.1.

Ward, N. B., 1972: The exploration of certain features of tornado dynamics using a laboratory model. *J. Atmos. Sci.*, **29**, 1194–1204, https://doi.org/10.1175/1520-0469(1972)029%3C1194:TEOCFO%3E2.0.CO;2.

Wicker, L. J., and W. C. Skamarock, 2002: Time-splitting methods for elastic models using forward time schemes. *Mon. Wea. Rev.*, **130**, 2088–2097, https://doi.org/10.1175/1520-0493(2002)130%3C2088:TSMFEM%3E2.0.CO;2.

Wilhelmson, R. B., and C.-S. Chen, 1982: A simulation of the development of successive cells along a cold outflow boundary. *J. Atmos. Sci.*, **39**, 1466–1483, https://doi.org/10.1175/1520-0469(1982)039%3C1466:ASOTDO%3E2.0.CO;2.

WMO, 2023: Guide to Meteorological Instruments and Methods of Observation, Vol. 1. World Meteorological Organization, 551 pp.

Wyngaard, J. C., 2010: *Turbulence in the Atmosphere.* Cambridge University Press, 393 pp., https://doi.org/10.1002/met.220.

Xue, M., M. Hu, and A. D. Schenkman, 2014: Numerical prediction of the 8 May 2003 Oklahoma City tornadic supercell and embedded tornado using ARPS with the assimilation of WSR-88D data. *Wea. Forecasting*, **29**, 39–62, https://doi.org/10.1175/WAF-D-13-00029.1.